

Preliminary Sizing Method for Hybrid-Electric Distributed-Propulsion Aircraft

de Vries, Reynard; Brown, Malcom; Vos, Roelof

DOI

[10.2514/1.C035388](https://doi.org/10.2514/1.C035388)

Publication date

2019

Document Version

Accepted author manuscript

Published in

Journal of Aircraft: devoted to aeronautical science and technology

Citation (APA)

de Vries, R., Brown, M., & Vos, R. (2019). Preliminary Sizing Method for Hybrid-Electric Distributed-Propulsion Aircraft. *Journal of Aircraft: devoted to aeronautical science and technology*, 56(6), 2172-2188. Advance online publication. <https://doi.org/10.2514/1.C035388>

Important note

To cite this publication, please use the final published version (if applicable). Please check the document version above.

Copyright

Other than for strictly personal use, it is not permitted to download, forward or distribute the text or part of it, without the consent of the author(s) and/or copyright holder(s), unless the work is under an open content license such as Creative Commons.

Takedown policy

Please contact us and provide details if you believe this document breaches copyrights. We will remove access to the work immediately and investigate your claim.

Preliminary Sizing Method for Hybrid-Electric Distributed-Propulsion Aircraft

Reynard de Vries*, Malcom Brown† and Roelof Vos‡
Delft University of Technology, Delft, South-Holland, 2629HS, The Netherlands

The use of hybrid-electric propulsion (HEP) entails several potential benefits such as the distribution of power along the airframe, which enables synergistic configurations with improved aerodynamic and propulsive efficiency. This article presents a comprehensive preliminary sizing method suitable for the conceptual design process of hybrid-electric aircraft, taking into account the powertrain architecture and associated propulsion–airframe integration effects. To this end, the flight-performance equations are modified to account for aero-propulsive interaction. A series of component-oriented constraint-diagrams are used to provide a visual representation of the design space. A HEP-compatible mission analysis and weight estimation are then carried out to compute the wing area, powerplant size, and take-off weight. The resulting method is applicable to a wide range of electric and hybrid-electric aircraft configurations and can be used to estimate the optimal power-control profiles. For demonstration purposes, the method is applied a regional HEP aircraft featuring leading-edge distributed-propulsion (DP). Three powertrain architectures are compared, showing how the aero-propulsive effects are included in the model. Results indicate that DP significantly increases wing loading and improves the cruise lift-to-drag ratio by 6%, although the growth in aircraft weight leads to an energy consumption increase of 3% for the considered mission.

Nomenclature

a	=	Axial induction factor [-]
A	=	Wing aspect ratio [-]
b	=	Wing span [m]
c	=	Chord [m] or climb rate [m/s]
C_D	=	Drag coefficient, $D/(q_\infty S)$ [-]
c_f	=	Sectional skin friction coefficient [-]
C_L	=	Lift coefficient, $L/(q_\infty S)$ [-]

*PhD Candidate, Faculty of Aerospace Engineering, R.deVries@tudelft.nl, AIAA member.

†Graduate Researcher, Faculty of Aerospace Engineering, M.T.H.Brown@tudelft.nl.

‡Assistant Professor, Faculty of Aerospace Engineering, R.Vos@tudelft.nl, Associate fellow AIAA.

c_l	=	Sectional lift coefficient [-]
D	=	Drag [N] or diameter [m]
e	=	Oswald factor [-] or specific energy [Wh/kg]
f_w	=	Aircraft weight fraction, W/W_{TO} [-]
g	=	Gravitational acceleration [m/s^2]
h	=	Altitude [m]
L	=	Lift [N]
m	=	Mass [kg]
M	=	Mach number [-]
n	=	Load factor [-]
N	=	Number of components [-]
P	=	Power [W]
PREE	=	Payload-range energy efficiency [-]
q_∞	=	Freestream dynamic pressure, $0.5\rho V^2$ [Pa]
R	=	Radius [m] or range [m]
S	=	Wing reference area [m^2]
t	=	Time [s]
T	=	Thrust [N]
T_c	=	Thrust coefficient, $T_P/(\rho V^2 D_p^2)$ [-]
V	=	Velocity [m/s]
W	=	Weight, $m \cdot g$ [N]
x	=	Axial position [m]
α	=	Angle of attack [rad]
β	=	Slipstream correction factor [-]
γ	=	Flight path angle [rad]
Δy	=	Lateral clearance between propulsors as a fraction of propulsor diameter [-]
ΔY	=	Span fraction occupied by distributed-propulsion system [-]
$\Delta()$	=	Change in aerodynamic force or efficiency due to aero-propulsive interaction
η	=	Conversion or transmission efficiency [-]
$\Lambda_{c/2}$	=	Wing half-chord sweep angle [rad]
μ	=	Bank angle [rad]
ξ	=	Throttle setting [-]
ρ	=	Atmospheric density [kg/m^3]
Φ	=	Supplied power ratio [-]
φ	=	Shaft power ratio [-]

χ = Thrust ratio of DP system, T_{dp}/T [-]

ω = Maneuver turn rate [rad/s]

Subscripts

0 = Zero-lift conditions

1 = Primary powertrain branch

2 = Secondary powertrain branch

airframe = Aircraft excluding propulsion system

bat = Battery

conv = Conventional propulsion system

cr = Cruise

dp = Distributed-propulsion system

e = Electrical path

eq = Equilibrium

EM = Electrical machine

f = Fuel

gb = Gearbox (path)

GB = Gearbox (component)

gt = Gas turbine (path)

GT = Gas turbine (component)

i = Lift-induced

isolated = Uninstalled configuration

max = Maximum

miss = Nominal mission (i.e. excluding diversion and reserves)

OE = Operative empty

OE' = Operative empty excluding wing and powertrain

p = Propulsive

P = Propulsor

PL = Payload

PM = Power management and distribution system

pt = Powertrain

ref = Reference aircraft

s = Shaft

SLS = Sea-level static conditions

turn = Sustained turn maneuver

TO = Take-off

w = Wing
 X' = Axial component
 Y' = Lateral component
 Z' = Vertical component

I. Introduction

In order to meet the stringent sustainability goals established by NASA [1] and the European Commission [2], numerous aircraft concepts featuring distributed propulsion have appeared in the last decade [3–13]. Distributed-propulsion systems promise improvements in aero-propulsive efficiency through, for example, reduced wing area [3, 8] or increased effective bypass ratio [4, 13]. This recent growth in distributed-propulsion concepts can be attributed to the development of hybrid-electric powertrains. While *distributed propulsion* (DP) implies spreading the propulsive elements (i.e., fans, propellers, or jets) over the airframe in a beneficial manner [14, 15], *hybrid-electric propulsion* (HEP) refers to the use of two energy types (electrical and chemical) in the generation and transmission of power. Although HEP can be used with different propulsion-system layouts, it presents a synergistic benefit when combined with distributed propulsion, due to the versatility that electrical systems offer when it comes to distributing power to the different locations on the airframe. This combination is referred to as hybrid-electric distributed propulsion (HEDP).

Despite the large amount of ongoing research related to hybrid-electric propulsion, little information is available regarding the clean-sheet design process of HEDP aircraft. In many cases, design studies analyze the hybrid-electric powertrain in detail starting from a predefined aircraft configuration [12, 16, 17], often maintaining the take-off weight constant [18–20]. Other studies have formulated more generalized conceptual sizing methods for HEP aircraft [20–28], but do not integrate the aero-propulsive interaction effects in the process. These effects cannot be neglected for DP configurations, since they have a large impact on wing and powertrain sizing [3, 29] and, hence, on the overall design of the aircraft. Thus, there is a need to establish a systematic sizing method capable of rapidly exploring the design space and performing trade-off studies and sensitivity analyses for such configurations. The goal of this article is therefore to present a new conceptual design method which sizes the wing, propulsion system, and take-off mass of aircraft featuring HEDP systems.

To this end, the traditional preliminary sizing methods [30–32] are expanded to account for both the hybrid-electric powertrain and the aero-propulsive effects of the associated propulsion system. The method is described in Section II. It is subsequently applied to a regional transport aircraft in Section III, in order to demonstrate the versatility of the method and the potential benefit of HEDP. Even though the examples described in this paper focus on wing-mounted DP systems, the rationale followed in this process can easily be extended to other novel propulsion-system layouts such as tip-mounted propellers or boundary-layer-ingestion systems.

II. Aircraft Sizing Methodology

This section describes how the wing area, installed power, and aircraft weight can be computed based on a series of top-level requirements and design parameters. The approach consists of four steps. First, the conventional thrust, lift, and drag decompositions of the aircraft are modified to account for the aerodynamic interaction between the airframe and the propulsors. This leads to a set of modified flight-performance constraint equations, which are collected in a propulsive power-loading diagram, as explained in Sec. II.A. Secondly, a powertrain model is formulated which converts the propulsive power-loading diagram into a series of powertrain component-oriented power-loading diagrams. The powertrain model is described in Sec. II.B. Based on these constraint diagrams, the designer must select a design point in terms of wing loading and power loading. Subsequently, the battery and fuel energy requirements are calculated for an assumed take-off mass (TOM) by analyzing the mission for a set of power-control profiles specified by the designer (Sec. II.C). Finally, with the power requirements obtained from the constraint diagrams and the energy requirements obtained from the mission analysis, the aircraft mass is estimated using a modified Class-I weight breakdown (Sec. II.D). The mission analysis and weight estimation modules are then evaluated iteratively until the TOM converges.

A. Sizing for Power: Performance Constraints

The first step in the sizing process is to determine the design wing-loading and power loading of the HEDP aircraft. These aircraft can feature multiple propulsion systems. In this context, a “propulsion system” is defined as a set of identical propulsive elements which have an equal impact on aircraft performance, such as for example an array of propellers distributed along the leading edge of the wing, or a pair of ducted fans. The propulsive elements are generally propellers, jets, or fans, and are indistinctly referred to as “propulsors” in this study. In many cases, at least one of the propulsion systems has an appreciable effect on the aerodynamic performance of the airframe or vice versa. This effect must be considered in the lift and drag decomposition of the aircraft (Sec. II.A.1), which affects the performance equations (Sec. II.A.2) and the resulting constraint diagram (Sec. II.A.3).

1. Thrust, Lift and Drag Decomposition

Due to the aero-propulsive interaction that takes place between the propulsors and the airframe, the aerodynamic performance of the system differs from the combined performance of the two individual components. For highly-integrated propulsion-systems such as distributed propulsion, it is necessary to estimate the forces generated by the installed system, or, more specifically, to estimate the difference between these forces and the ones that the airframe and propulsors would generate separately. Although the rationale followed in the following paragraphs can be extended to a generic number of propulsion systems, for simplicity it is assumed that the aircraft features a maximum of two types of propulsion system. In this case, the total thrust of the aircraft T can be expressed as

$$T = T_{\text{conv}} + T_{\text{dp}}, \quad (1)$$

where T_{conv} is the thrust generated by a propulsion system that has no appreciable impact on airframe performance, and T_{dp} is the thrust generated by a (distributed) propulsion system which presents strong interaction effects with the airframe.

There are several ways to account for the effect of the airframe on propulsor performance. The first is to evaluate the changes in propulsor thrust due to the presence of different elements such as the wing, nacelle, fuselage, and so on [33]. For configurations with significant inflow distortion such as boundary-layer ingestion, on the other hand, an integral system-level approach is required, using for example the power-saving coefficient [34, 35] or power-balance methods [36, 37]. In any case, since the hybrid-electric powertrain is modeled in terms of power balances (see Sec. II.B), it is preferable to express the interaction effects in terms of the propulsive efficiency of the distributed propulsion system η_{dp} :

$$\eta_{\text{dp}} = \frac{T_{\text{dp}}V}{P_{\text{s,dp}}} = \eta_{\text{dp,isolated}} + \Delta\eta_{\text{dp}}(T_{\text{dp}}, L_{\text{airframe}}, S, \dots). \quad (2)$$

Here $\eta_{\text{dp,isolated}}$ is the propulsive efficiency that these propulsors would have in absence of any other body, and $\Delta\eta_{\text{dp}}$ refers to the change in propulsive efficiency when installed on the aircraft. $\Delta\eta_{\text{dp}}$ may depend on geometrical parameters of the wing such as its reference area, as well as on aerodynamic parameters such as L_{airframe} , which is the lift generated by the aircraft when no thrust is produced. The airframe lift can be related to the total lift generated by the aircraft L through

$$L = L_{\text{airframe}} + \Delta L(T_{\text{dp}}, L_{\text{airframe}}, S, \dots), \quad (3)$$

where ΔL is the increase in aircraft lift due to the thrust generated by the propulsors. ΔL depends on thrust of the distributed propulsion system and other operational and geometrical parameters of the aircraft, and does not include the effective lift increase due to thrust vectoring.

The effect of aero-propulsive interaction on the overall drag of the aircraft is included as follows:

$$D = D_0 + \Delta D_0(T_{\text{dp}}, S, \dots) + D_i(L_{\text{airframe}}) + \Delta D_i(T_{\text{dp}}, L_{\text{airframe}}, S, \dots), \quad (4)$$

where D_0 is the zero-lift drag of the aircraft when no DP system is present, and ΔD_0 is the increase in zero-lift drag due to the DP system. This increase can be caused by interaction of the airframe with jets or slipstreams at zero lift, by variations in angle of attack in order to maintain zero lift, or by changes in wetted area due to pylons, nacelles, and other external elements of the propulsion-system installation. Additionally, D_i is the lift-induced drag of the airframe without propulsion system, and ΔD_i is the change in lift-induced drag due to thrust, that is, the difference between the drag

of the complete aircraft with the propulsor at a determined thrust setting, and the drag that would exist at $T_{dp} = 0$ for the same total lift value. For the lift-induced drag coefficient of the airframe, a parabolic lift polar is assumed (i.e., $C_{Di} = C_{L_{airframe}}^2 / (\pi Ae)$). Although different drag breakdowns exist, this simplified approach has been taken because it clearly identifies the contribution of the installation effects.

In order to incorporate the aero-propulsive interaction effects in the sizing process, these ‘‘Delta’’ terms (lift, drag, and propulsive efficiency) have to be estimated. Since an accurate estimation of the Delta components requires detailed aerodynamic analyses, they are often only included in the later stages of the design loop. For DP systems and other novel propulsion-system layouts, these effects cannot be neglected, and therefore simplified aerodynamic models or surrogate models are required. An example of how this can be done for leading-edge-mounted propellers is provided in Sec. III.

2. Derivation of Point Performance Equations

The main forces acting on the aircraft are represented in Fig. 1. Here it is assumed that T_{conv} is aligned with the velocity vector for simplicity, while the thrust vector of the DP system can be deflected an angle α_p if, for example, the propulsors are installed on a flap, or if the jet or slipstream is deflected (see e.g. Schiltgen et al. [6]). The velocity vector is assumed to be aligned with the X' axis. By applying Newton’s second law along the X' , Y' and Z' axes respectively, one obtains the following equilibrium equations:

$$T_{conv} + T_{dp} \cos \alpha_p - W \sin \gamma - D = \frac{W}{g} \frac{dV_{X'}}{dt}, \quad (5a)$$

$$L \sin \mu + T_{dp} \sin \alpha_p \sin \mu = \frac{W}{g} \frac{dV_{Y'}}{dt}, \quad (5b)$$

$$L \cos \mu + T_{dp} \sin \alpha_p \cos \mu - W \cos \gamma = \frac{W}{g} \frac{dV_{Z'}}{dt}, \quad (5c)$$

where the flight path angle γ of the aircraft can be related to the climb rate $c = dh/dt$ through

$$\sin \gamma = \frac{c}{V}. \quad (6)$$

Defining the ratio between the thrust of the DP array and the total thrust of the aircraft as $\chi = T_{dp}/T$, the force equilibrium along the X' axis (Eq. 5a) can be expressed as

$$\frac{T}{W} = \frac{1}{1 - \chi(1 - \cos \alpha_p)} \left(\frac{D}{W} + \frac{c}{V} + \frac{1}{g} \frac{dV}{dt} \right), \quad (7)$$

where the term on left hand side of the equation is the total thrust-to-weight ratio of the aircraft. By reorganizing terms, applying the lift and drag breakdowns given by Eqs. 3 and 4, and expressing the contributions as non-dimensional coefficients, the equilibrium of forces along the X' and Z' axes can be expressed as:

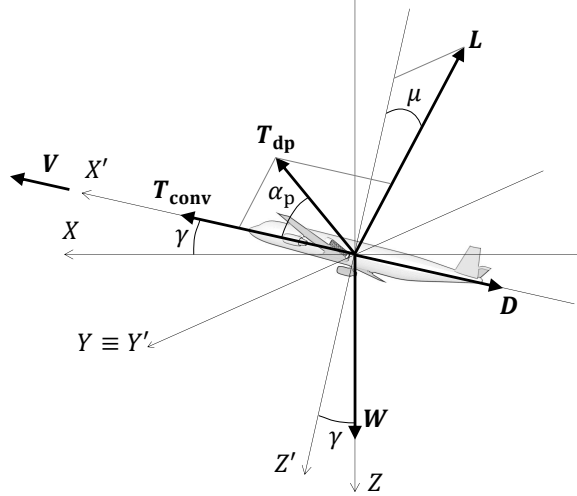


Fig. 1 Schematic representation of the forces acting on the aircraft point model.

$$\frac{T}{W} = \frac{\frac{q_\infty}{(W/S)} \left[C_{D_0} + \Delta C_{D_0} \left(\chi \frac{T}{W}, \frac{W}{S}, \dots \right) + \frac{C_{L_{\text{airframe}}}^2}{\pi A e} + \Delta C_{D_i} \left(\chi \frac{T}{W}, C_{L_{\text{airframe}}}, \frac{W}{S}, \dots \right) \right] + \frac{c}{V} + \frac{1}{g} \frac{dV}{dt}}{1 - \chi(1 - \cos \alpha_p)}, \quad (8)$$

$$\frac{W}{S} = \frac{q_\infty \cos \mu \left[C_{L_{\text{airframe}}} + \Delta C_L \left(\chi \frac{T}{W}, C_{L_{\text{airframe}}}, \frac{W}{S}, \dots \right) \right]}{\sqrt{1 - \left(\frac{c}{V} \right)^2} - \chi \left(\frac{T}{W} \right) \sin \alpha_p \cos \mu + \frac{1}{g} \frac{dV_{Z'}}{dt}}. \quad (9)$$

Equations 8 and 9 constitute the point performance equations used to construct the constraint diagram of a HEDP aircraft. Since performance constraints are typically evaluated for steady symmetric flight or coordinated turns in the horizontal plane, the terms dV/dt and $dV_{Z'}/dt$ are generally equal to zero. Sustained-turn maneuvers can be solved directly using Equations 8 and 9 if the bank angle is known. However, if the turn radius of the maneuver is given as a performance requirement instead, the bank angle has to be computed from the equilibrium of forces along the Y' axis. In this case, $dV_{Y'}/dt$ represents the centrifugal acceleration of the aircraft, and Eq. 5b can be rewritten as

$$\sin \mu = \frac{\frac{1}{g} \frac{V^2}{R_{\text{turn}}}}{\frac{q_\infty}{W/S} \left[C_{L_{\text{airframe}}} + \Delta C_L \left(\chi \frac{T}{W}, C_{L_{\text{airframe}}}, \frac{W}{S}, \dots \right) \right] + \chi \sin \alpha_p \left(\frac{T}{W} \right)}. \quad (10)$$

If, on the other hand, the turn rate or load factor of the maneuver are specified, these can be related to the turn radius through $\omega = V/R_{\text{turn}}$ and $n = \sqrt{1 + (V^2/gR_{\text{turn}})^2}$, respectively.

Given that the aircraft size is unknown at this stage, it is important to express the ‘‘Delta’’ terms as a function of normalized variables such as the thrust coefficient T_c or aerodynamic force coefficients. These can in turn be related to T/W and W/S (see Sec. III.A.1), and thus the performance equations can be solved without knowing the actual weight

of the aircraft. For conventional aircraft, the “Delta” terms are zero and the airframe lift coefficient can be related to wing loading directly through $C_{L_{\text{airframe}}} = (W/S)/q_{\infty}$, and therefore T/W can explicitly be computed as a function of wing loading for a given flight condition. However, when the aero-propulsive effects are considered during equilibrium flight, lift depends on thrust and vice versa. Hence, given that $\Delta C_L, \Delta C_{D_0}, \Delta C_{D_i} = f(\chi(T/W), C_{L_{\text{airframe}}}, (W/S), \dots)$ can be arbitrarily complicated functions, Eqs. 8 and 9 must be solved iteratively.

3. Constructing the Performance Constraint Diagram

For a given flight condition and airframe lift coefficient, Eqs. 8 and 9 generate the two solid curves shown Fig. 2. The intersection of these curves gives the equilibrium flight point $[(W/S)_{\text{eq}}, (T/W)_{\text{eq}}]$, that is, the combination of T/W and W/S where the required flight condition is satisfied without any additional accelerations. Along the “ Z' -equilibrium” curve, the aircraft presents no acceleration in Z' direction, and thus it can climb or accelerate in X' direction if the excess power is positive ($T/W > (T/W)_{\text{eq}}$), or descend or decelerate if it is negative ($T/W < (T/W)_{\text{eq}}$). Analogously, the “ X' -equilibrium” curve represents the loci of points of zero excess power. Along this curve, the aircraft accelerates in the negative Z' direction if $T/W > (T/W)_{\text{eq}}$, or in positive Z' direction if $T/W < (T/W)_{\text{eq}}$. The potential benefit of distributed propulsion can clearly be identified in Fig. 2: for a given airframe lift coefficient, the wing loading of the aircraft can be increased from $(W/S)_{T_{\text{dp}}=0}$ to $(W/S)_{\text{eq}}$, if $\Delta C_L > 0$.

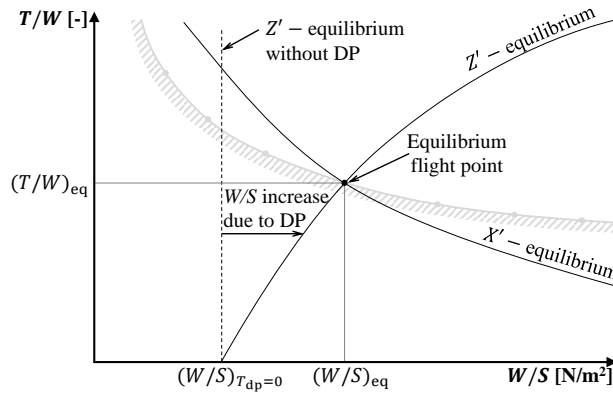


Fig. 2 Notional wing-loading versus thrust-to-weight-ratio diagram indicating the curves obtained from the equilibrium of forces along the X' axis (Eq. 8) and Z' axis (Eq. 9).

The solution of Eqs. 8 and 9 provides a single point in the diagram. By parametrically varying one of the variables, the equations can be solved to obtain a constraint curve, as indicated by the gray, hashed curve in Fig. 2. For most constraints, either the airframe lift coefficient or the flight speed are varied to obtain the points of this curve. Taking this into consideration, four types of performance constraints can be distinguished:

- Constraints at constant flight speed. As the assumed airframe lift coefficient increases while keeping the flight speed constant, a smaller wing (i.e. higher wing loading) is required to generate the same total lift.
- Constraints at constant airframe lift coefficient. This occurs when a stall margin has to be maintained. For example,

if a climb gradient requirement must be met at 1.4 times the reference stall speed, then the aircraft must be able to fly at $C_{L_{\max}}/1.4^2$, where $C_{L_{\max}}$ is the total maximum lift coefficient (including aero-propulsive effects*). In this case, the resulting velocity at which the maneuver must be performed increases with increasing wing loading.

- Constraints at fixed flight speed and airframe lift coefficient. An aircraft must be able to, for example, achieve a determined stall speed at $C_{L_{\max}}$. Since both the velocity and lift coefficient are fixed, a single point in the diagram is obtained. This implies that the maximum wing loading can only be reached at a single thrust-to-weight ratio. If the pilot were to decrease the thrust setting at maximum wing loading, the aircraft would stall not only due to its deceleration, but also because the change in lift due to thrust (ΔC_L) would decrease. Since the thrust required for this performance constraint is, in general, not a sizing condition, the engines must be set to a predetermined thrust setting once the powertrain has been sized by one of the other, more limiting constraints. Thus, for resemblance with conventional wing-loading diagrams, in this article a vertical line is drawn at the wing loading corresponding to the point obtained. However, if the DP system is sized in landing conditions—as may be the case for concepts comparable to e.g. the X-57 demonstrator [3]—then the installed thrust must correspond exactly to the T/W obtained at this point. In that case, the designer can still opt for a lower wing loading ($C_L < C_{L_{\max}}$), but then the performance requirement becomes a constant-flight-speed constraint.
- Semi-empirical constraints. During take-off and landing, Eqs. 5a, 5b and 5c are not applicable due to the forces exerted on the runway surface. Hence, semi-empirical methods [30, 32] are used to determine the take-off distance and landing distance constraints. In the example provided in Sec. III, the take-off-parameter (TOP) described by Raymer [32] is used.

For HEDP aircraft, a power-loading diagram is preferred over a thrust-to-weight ratio diagram, since the powertrain components are modeled in terms of power (see Sec. II.B). The thrust-to-weight ratios obtained from Eqs. 8 and 9 can be expressed as power-loading (W/P_p) values using:

$$\frac{W}{P_p} = \frac{1}{V(T/W)}. \quad (11)$$

Subsequently, each curve has to be corrected to take-off weight (TOW), in order to compare the different constraints in equal conditions. To this end, a weight fraction f_W is assumed for each flight condition, such that $(W_{TO}/P) = (W/P)/f_W$. After applying this weight correction, the *propulsive* power-loading diagram is obtained. In traditional power-loading diagrams, the *shaft* power is used on the Y -axis of the power-loading diagram, since this determines the size of the gas turbine. However, for HEP aircraft, multiple components exist, each of which can be sized by different requirements. Therefore, the propulsive power-loading diagram must be translated into a series of component-oriented power-loading diagrams, creating one power-loading diagram per component of the powertrain.

*In this article it is assumed that future airworthiness regulations will change such that the performance requirements can be met in powered conditions, instead of in engine-idle conditions. Although this is change currently subject to debate [38], it should be kept in mind that some of the benefits of distributed-propulsion systems cannot be achieved with the current regulations.

B. Hybrid-Electric Powertrain Modeling

This section presents a simplified analytical model used to compute the power required from any element of the powertrain for a given propulsive power requirement and power-control strategy. Several prerequisites are considered for the model. Firstly, it must require only a limited amount of input variables which are known in the preliminary sizing phase. Secondly, it has to be sensitive to different powertrain architectures, including those which present two distinct propulsion systems. Thirdly, it must account for component failure, and be compatible with the charging of batteries, as well as energy harvesting. Finally, it should be sensitive to a series of power-control parameters which allow a posterior analysis and optimization of power settings along the mission.

In order to be able to meet all these prerequisites simultaneously, a series of simplifications are required. The system is treated as steady-state, and a constant conversion/transmission efficiency is assumed per component. Additionally, the effect of battery state-of-charge and system voltage are not considered. Furthermore, the cables and thermal management systems are not explicitly included in the model. Although these simplifications limit the accuracy and applicability of the model, the approach is considered sensitive enough for the preliminary sizing phase.

1. Hybrid-Electric Powertrain Architectures

This study considers a set of predefined powertrain architectures, based on the classification of the National Academy of Engineering [39]. These architectures are shown in the first six figures of Fig. 3, also including a conventional powertrain for reference. The simplified representations include energy sources, nodes, components which transform one type of power into another, and the power paths that connect these elements. Components such as converters or transformers are not explicitly modeled, since they do not change the type of power transmitted. Nevertheless, the effect of converters (i.e., inverters and rectifiers) can be accounted for by including their weight correlations and efficiency losses in the associated electrical machine (EM) elements. Similarly, in first approximation, the weight and efficiency of other elements of the electrical grid can be grouped in the power management and distribution (PMAD, or “PM”) element. The components are divided into the elements which constitute the “primary” powertrain, and those that constitute the “secondary” powertrain. The primary components are, directly or indirectly, mechanically coupled to the gas turbine. The secondary components include the devices which power the electrically-driven propulsion system. The primary and secondary branches of the powertrain contain N_1 and N_2 identical instances of each component, respectively.

Closer inspection of the first six powertrain configurations shown in Fig. 3 reveals that the first five are, in essence, limit cases of the sixth (the serial/parallel partial hybrid, SPPH). Therefore, with the correct parametrization, the SPPH architecture can be used as a generic model which can be solved for any other architecture as well. In other words, independently of the chosen architecture, the same set of equations can be used to compute component powers, and no architecture-specific equations have to be derived like in other sizing methods [28]. After a more detailed analysis of

the SPPH, three additional limit cases are identified (Configurations 7–9), which do not use fuel. Thus, the model is applicable to conventional, hybrid-electric, and fully-electric powertrains.

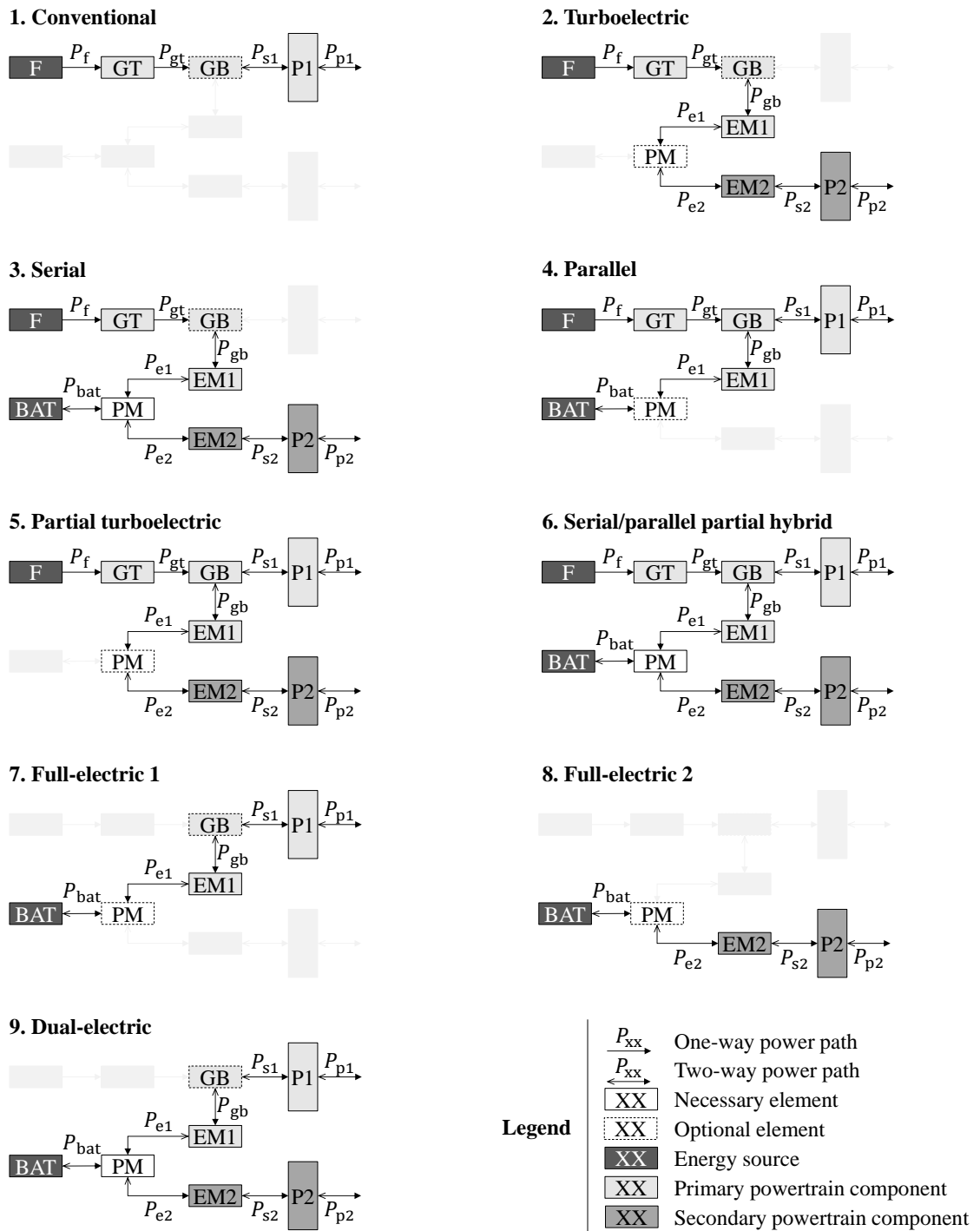


Fig. 3 Simplified models of the nine powertrain architectures considered in this study. Filled arrowheads indicate the transmission direction corresponding to positive power values.

2. Definition of Power Control Parameters

The SPPH architecture contains two nodes: a gearbox and a PMAD system. Therefore, one can already anticipate that two parameters are necessary in order to completely define the power shares of the system, in addition to one extensive parameter which dictates how much power the system must actually produce. The authors of previous studies [12, 21, 24, 40] have used different parameters to describe the powertrain, and it appears no consensus has been reached with respect to the nomenclature and definition of these variables. Consequently, the parameters proposed here are based on previous definitions, but have been modified such that specific combinations of the power-control parameters can define the powertrain architecture.

The first parameter is the *supplied power ratio*, which was originally defined by Isikveren et al. [21] and can be expressed as

$$\Phi = \frac{P_{\text{bat}}}{P_{\text{bat}} + P_{\text{f}}}. \quad (12)$$

The supplied power ratio represents the amount of power drawn from the electrical energy source (batteries) with respect to the total amount of power drawn from all energy sources (battery plus fuel, in this case) for a given point along the mission. Hence, this parameter is only non-zero for powertrains containing batteries (configurations 3, 4 and 6–9). In normal operation, the battery is discharging and thus $\Phi \in [0, 1]$. However, if the battery is being charged ($P_{\text{bat}} < 0$), this parameter is negative or greater than one.

The second power-control parameter is the *shaft power ratio*, which represents the amount of shaft power produced by the secondary electrical machines with respect to the total amount of shaft power produced in a given flight condition:

$$\varphi = \frac{P_{s2}}{P_{s2} + P_{s1}}. \quad (13)$$

Analogously to the supplied power ratio, the shaft power ratio belongs to the interval $\varphi \in [0, 1]$ during normal operation (when both propulsion systems are generating thrust), but is negative or greater than 1 if one or both of the propulsion systems are windmilling (i.e., extracting energy from the flow). The relations between the two power-control parameters and the nine powertrain layouts considered are collected in Table 1.

Apart from these two power control parameters, the conventional gas-turbine throttle is defined as

$$\xi_{\text{GT}} = \frac{P_{\text{GT}}}{P_{\text{GT,max}}}, \quad (14)$$

which represents the power produced by the gas turbine with respect to the maximum power it can produce in the given flight condition. This power can in turn be related to the installed sea-level static power of the gas turbine $P_{\text{GT,max,SLS}}$ by means of an altitude and velocity lapse. In this paper, the altitude lapse provided by Ruijgrok [41] is applied, and the velocity lapse is neglected. For the fully-electric architectures (Configurations 7–9), where no gas turbine is used, an analogous “electrical machine throttle” is used instead:

Table 1 Supplied power ratio and shaft power ratio values associated to each architecture. A dot (·) indicates any value can be used.

Configuration	Φ	φ
1. Conventional	0	0
2. Turboelectric	0	1
3. Serial	·	1
4. Parallel	·	0
5. Partial TE	0	·
6. S/P partial hybrid	·	·
7. Full-electric 1	1	0
8. Full-electric 2	1	1
9. Dual-electric	1	·

$$\xi_{EM} = \frac{P_{EM}}{P_{EM,max}}. \quad (15)$$

In Eqs. 14 and 15 the subscripts contain upper-case letters. These refer to a *component* of the powertrain, while lower-case letters refer to a *power path* (indicated by arrows in Fig. 3). Although the “installed” gas turbine power evidently refers to the shaft power it can produce (i.e. $P_{GT} = P_{gt}$), for an electrical machine this distinction is necessary. For example, the “installed” electrical machine power P_{EM2} could either be equal to P_{e2} or P_{s2} , depending on whether it is acting as an electric motor or as a generator.

Finally, it is necessary to link the power-control parameters to the performance constraint equations derived in Sec. II.A.2. In this process, two thrust sources were assumed, T_{conv} and T_{dp} . Logically, the use of two thrust sources is only compatible with powertrain architectures that present two types of propulsion system (i.e., configurations 5, 6, and 9). For the other architectures, either T_{conv} or T_{dp} has to be zero. If the aircraft does present two propulsion systems, then the thrust ratio χ can be related to the shaft power ratio φ through

$$\chi = \begin{cases} \frac{1}{1 + \frac{\eta_{p2}}{\eta_{p1}} \left(\frac{\varphi}{1 - \varphi} \right)}, & \text{if the DP system belongs to the primary powertrain branch,} \\ \frac{1}{1 + \frac{\eta_{p1}}{\eta_{p2}} \left(\frac{1 - \varphi}{\varphi} \right)}, & \text{if the DP system belongs to the secondary powertrain branch,} \end{cases} \quad (16)$$

where η_{p1} and η_{p2} are the propulsive efficiencies of the propulsors of the primary and secondary powertrain branches, respectively. The propulsive efficiency given by Eq. 2 corresponds to either η_{p1} or η_{p2} , depending on whether the DP system is installed on the primary or secondary powertrain branch. With Eq. 16 it is evident that χ and φ represent

the same degree of freedom, but χ refers to the *propulsive* power share of the DP system (which can correspond to either the primary or secondary powertrain branch), while φ refers to the *shaft* power share of the secondary, electrically-driven, propulsor system. Thus, if φ is not in the interval [0,1] because one or both of the propulsion systems are harvesting energy, then χ is also negative or greater than one. Consequently, the thrust-to-weight ratio obtained from the performance equations will change accordingly.

3. Solving the Powertrain Equations

The powertrain model has ten unknowns, corresponding to the ten power paths shown in Fig. 3.6. Thus, ten equations are necessary to solve the system. The first seven can be obtained by applying a power balance across each component. For a generic component, this equation is expressed as:

$$\sum P_{\text{out}} = \eta \sum P_{\text{in}}, \quad (17)$$

where the left-hand side indicates the summation of power paths flowing “out” of the component, and the right-hand side represents the summation of power paths flowing “in” to the component, multiplied by the conversion efficiency of the component, η .

Three additional equations or values are required. This ties in to the discussion of Sec. II.B.2, which stated that three parameters have to be specified in order to define the complete behavior of the powertrain. For example, Φ (which relates P_{bat} to P_f), φ (which relates P_{s1} to P_{s2}), and the total required propulsive power $P_p = P_{p1} + P_{p2}$ can be specified. The set of linear equations can then be expressed as

$$\begin{bmatrix} -\eta_{GT} & 1 & 0 & 0 & 0 & 0 & 0 & 0 & 0 & 0 \\ 0 & -\eta_{GB} & 1 & 1 & 0 & 0 & 0 & 0 & 0 & 0 \\ 0 & 0 & 0 & -\eta_{P1} & 0 & 0 & 0 & 0 & 1 & 0 \\ 0 & 0 & -\eta_{EM1} & 0 & 1 & 0 & 0 & 0 & 0 & 0 \\ 0 & 0 & 0 & 0 & -\eta_{PM} & -\eta_{PM} & 1 & 0 & 0 & 0 \\ 0 & 0 & 0 & 0 & 0 & 0 & -\eta_{EM2} & 1 & 0 & 0 \\ 0 & 0 & 0 & 0 & 0 & 0 & 0 & -\eta_{P2} & 0 & 1 \\ \Phi & 0 & 0 & 0 & 0 & (\Phi - 1) & 0 & 0 & 0 & 0 \\ 0 & 0 & 0 & \varphi & 0 & 0 & 0 & (\varphi - 1) & 0 & 0 \\ 0 & 0 & 0 & 0 & 0 & 0 & 0 & 0 & 1 & 1 \end{bmatrix} \cdot \begin{bmatrix} P_f \\ P_{gt} \\ P_{gb} \\ P_{s1} \\ P_{e1} \\ P_{bat} \\ P_{e2} \\ P_{s2} \\ P_{p1} \\ P_{p2} \end{bmatrix} = \begin{bmatrix} 0 \\ 0 \\ 0 \\ 0 \\ 0 \\ 0 \\ 0 \\ 0 \\ 0 \\ P_p \end{bmatrix}. \quad (18)$$

In Eq. 18, the first seven rows of the coefficient matrix correspond to the power balance equations across the gas turbine, gearbox, primary propulsor, primary electrical machine, PMAD, secondary electrical machine, and secondary propulsor, respectively. The last three rows correspond to the additional information provided. These three rows can be replaced by different equations, depending on what the designer wants to specify as input to the problem. For example, during the mission analysis, the three power-control parameters can be specified as input, and the resulting propulsive power

produced by the aircraft can be computed. However, if a configuration different than the SPPH is selected, then one or two of these equations will be fixed by Φ and/or φ (see Table 1). For example, if a turboelectric configuration is selected, then $\Phi = 0$ and $\varphi = 1$. In this case, rows 8 and 9 of Eq. 18 are readily determined, and the remaining degree of freedom must be specified in the last row.

The signs of the coefficients in Eq. 18 assume that the powers flow as indicated by the filled arrowheads in Fig. 3.6. If, for example, the primary electrical machine acts as an electric motor, providing power to the primary system, then P_{e1} and P_{gb} are negative. Under these conditions, the criteria of which power paths flow “in” and “out” of the component in Eq. 17 change. Therefore, the efficiency factor will appear in a different column of the coefficient matrix. This implies that the values in the coefficient matrix are not actually constants, but depend on the direction of the power flows, that is, on the sign of the solution variables. One possibility would be to assume a given direction of power flows and to solve the system iteratively, updating the coefficient matrix based on the sign of the solution of the previous iteration. However, this should be done with caution, since the solution presents discontinuities in gradient, and Φ and φ tend to infinity as $P_f \rightarrow -P_{bat}$ and $P_{s1} \rightarrow -P_{s2}$, respectively. A more effective approach is to assume a given direction of power flow, to construct and solve the corresponding matrix, and to verify the assumption thereafter. Closer inspection of the SPPH architecture reveals that in total nine possible operating modes exist. This conclusion can be drawn by considering that the gas turbine can only produce positive power, and that not all power paths connected to a given component can simultaneously flow in or out of that component. Although in a most generic sense all the different solutions have to be probed, in most practical applications the designer decides beforehand under which conditions the powertrain is operating. Moreover, the other, more simple powertrain architectures contain less possible operating modes, and thus only a limited number of these combinations have to be evaluated.

4. Sizing for Component Failure

When applying the powertrain model to the propulsive power-loading diagram, the inverse of power loading, $1/(W/P_p)$, can be used. In other words, the powers are computed per unit weight of the aircraft. However, some of the constraints in the diagram must be met in “one-engine-inoperative” (OEI) conditions. OEI is interpreted here as the failure of any one component of the powertrain. An exception is the PMAD, which is assumed to contain redundant buses, such that the failure of a component of the primary powertrain branch does not affect the secondary powertrain branch and vice versa. Thus, the effect of a single component failure can be accounted for by over-sizing all components of the branch where the failure occurs by a factor $N_1/(N_1 - 1)$ or $N_2/(N_2 - 1)$, depending on whether the failure occurs in the primary or secondary powertrain branch, respectively. This implies that a single propulsive-power constraint leads to two constraints in the component-power-loading diagrams in OEI conditions, depending on the powertrain branch in which the failure occurs.

The previous paragraph assumes that a single component of the powertrain will fail, as is traditionally assumed for conventional aircraft. However, in the case of DP systems, multiple instances of the components may be powered by the same source. As an example, consider a HEP aircraft with twelve electrically-driven fans, clustered in groups of three, such that if a connection fails in the PMAD, three electrical machines are lost simultaneously. In this case, the “OEI” sizing constraint must over-size each element of that powertrain branch by a factor $N_2/(N_2 - 3)$. It becomes evident that, in general, accurately sizing the electrical powertrain for all possible failure modes is a complicated and case-specific task, and is therefore not treated in depth in this preliminary sizing method. A designer can use this method as basis and gradually increase the fidelity of the modeling as the system architecture becomes more defined. Similarly, the effect of battery pack failure is not addressed in this study. Although a simple correction can be applied by multiplying the battery’s power requirements by a fraction $N_{\text{bat}}/(N_{\text{bat}} - 1)$, where N_{bat} is the number of independent battery packs, an accurate evaluation of battery failure would require a more detailed design and analysis of the electrical system.

Another important characteristic of powertrains with two energy sources is the ability to divert power from one branch to the other in case of component failure. For example, if one of two gas turbines fails, the other will not have to be over-sized by a factor 2, if the battery can supply additional power. This would, in essence, change the supplied power ratio during that flight condition. Therefore, although the re-routing of power in case of component failure is not explicitly included in the present method, it can be accounted for by correctly selecting the independent variables φ and Φ . The designer can do so through trial-and-error, or by means of an external optimization loop. Finally, it is worth noting that in case of component failure, the same total thrust is maintained in order to meet the performance requirement, and thus the aero-propulsive effects are assumed to remain unaffected. This is a valid assumption if ΔC_L , ΔC_D , and $\Delta \eta_p$ vary linearly with thrust. However, if the failure of a determined powertrain component has a significant impact on the aero-propulsive effects, then the delta terms of Eqs. 2–4 must include additional dependencies to reflect this.

C. Sizing for Energy: Mission Analysis

This step of the sizing process calculates the fuel and battery energy required for an assumed mission profile and take-off weight. Since, at this stage, the power-loading of each component has been determined, the installed power can readily be obtained with an assumed TOW value. For conventional aircraft, the fuel mass is commonly determined using the Breguet range equation [30, 31]. Analytical range formulae have been derived for hybrid-electric aircraft [12, 42, 43], but they are only applicable to a determined power-control strategy. Since the power-control profiles have a strong impact on block energy consumption [21], the energy sizing method must be applicable for generic power-control profiles. Therefore, no single analytical expression can be used, and a mission analysis is required.

For this reason, a numerical quasi-steady point-model is used, which analyses the instantaneous point performance of the aircraft at suitably small time intervals along the mission. For each time step, performance is assumed constant

and thus the battery energy and fuel energy consumed in the interval can be estimated by multiplying P_{bat} and P_f by the duration of the time interval. The power consumption at the energy sources is in turn related to the total propulsive power through the powertrain model described in Sec. II.B. Depending on the mission segment, the designer can either specify the required propulsive power and compute the necessary power-control parameters, or specify all three power-control parameters and compute the resulting excess power used to change altitude or velocity. The total propulsive power can be calculated as a function of the flight condition using Eqs. 8, 9 and 11. In this way, the aero-propulsive interaction effects are taken into account. Finally, the total energy requirements are computed by integrating the energy consumption per time interval along the entire mission.

D. Weight Estimation

For hybrid-electric aircraft, the operative empty weight (OEW) cannot be estimated using the traditional Class-I empirical correlations, since there is no weight database for HEP aircraft. The weight breakdown of these aircraft differs appreciably from conventional aircraft for several reasons. First of all, the battery weight has to be included in the total aircraft weight. Secondly, the weight of the powertrain is considerably higher for hybrid-electric propulsion systems (see for example Refs. [6–8, 20, 22, 44, 45]). Furthermore, in some cases, the wing loading can be significantly higher for HEP concepts [3], and therefore the wing weight fraction will not be comparable to conventional aircraft. Taking this into account, the TOW of the aircraft can be expressed as:

$$W_{\text{TO}} = W_{\text{OE}} + W_{\text{PL}} + W_f + W_{\text{bat}}, \quad (19)$$

where the fuel weight W_f is obtained from the mission analysis. The weight of the batteries W_{bat} can be determined by either energy or power requirements. Both should be evaluated in the sizing process, so as to assure both requirements are met. In terms of energy requirements, the total battery energy computed in the mission analysis can be divided by the specific energy of the batteries at pack level, e_{bat} , in order to obtain the battery mass. To this amount, a minimum SOC margin (typically around 20% [44, 46]) should be added to avoid limited power output or reducing the batteries' cycle life. The maximum power requirement, on the other hand, can be obtained from the design power-loading value obtained in the battery-power-loading diagram, together with an initial guess of the TOW, i.e. $P_{\text{bat}} = W_{\text{TO}}/(W_{\text{TO}}/P_{\text{bat}})$. This can then be converted into a minimum battery mass requirement if the battery's specific power at pack level is known. The specific energy and power at pack level can in turn be related to more accurate descriptors such as cell voltage, maximum discharge rate, or packaging efficiency if a battery model is available.

The OEW term of Eq. 19 should be further decomposed in order to distinguish the contribution of the powertrain W_{pt} , as evidenced in earlier studies [23, 25, 44]. Furthermore, as discussed previously, the contribution of the wing weight W_w should be isolated:

$$W_{OE} = W_{OE'} + W_w + W_{pt}. \quad (20)$$

In Eq. 20, $W_{OE'}$ is the operating empty weight excluding the powertrain and wing. This component can be estimated by calculating the OEW of a conventional reference aircraft using empirical correlations, and subtracting the weight that the wing and powerplant would have on that aircraft, i.e. $W_{OE'} = W_{OE,ref} - W_{w,ref} - W_{pt,ref}$. This assumes that the rest of the airframe is not significantly affected by incorporating a HEP or DP system. Although the accuracy of this assumption is debatable, more detail would imply going to a complete Class-II weight estimation, for which a more extensive description of the design would be required. The empirical correlations used in this paper for the wing, turboshaft, and operating empty weight of conventional aircraft are based on the books of Torenbeek [30], Roskam [31], and Raymer [32], respectively. The wing-loading value used to compute $W_{w,ref}$ is estimated by evaluating the stall speed constraint in absence of aero-propulsive interaction effects, in which case $(W/S)_{ref} = q_{\infty} C_{L_{max,airframe}}$.

Finally, the weight of the powertrain has to be estimated. If the specific power (kW/kg) or a power-to-weight correlation of each component of the corresponding powertrain architecture is known, then the complete powertrain weight can be estimated for a given TOW value, since the power required from each component is determined by its respective power-loading diagram. Since most of the mentioned component weights depend on the TOW of the aircraft, an iterative calculation is required. After converging on the TOW in the weight estimation module, the mission analysis can be employed to recompute the fuel and battery energy requirements, repeating the process until converging on a final TOW.

III. Demonstration: Leading-Edge Distributed-Propulsion Configurations

The derivations presented so far are applicable to HEP aircraft with generic propulsion-system layouts. This section demonstrates how the method can be applied to tube-and-wing aircraft featuring leading-edge distributed-propulsion systems. First, the aero-propulsive interaction model used to determine the ‘‘Delta’’ terms for such configurations is presented in Sec. III.A. Then, a set of hypothetical top-level requirements is defined in Sec. III.B, together with the assumed aircraft characteristics and design parameters. Furthermore, a power control strategy is chosen and discussed in Sec. III.C. Finally, in Sec. III.D a conventional configuration is compared to reference aircraft data and two hybrid-electric concepts, showing the potential benefits and penalties of these HEP aircraft.

A. Aero-Propulsive Interaction Model

A series of ‘‘Delta’’ terms (ΔC_L , ΔC_{D_0} , ΔC_{D_i} , and $\Delta \eta_{dp}$) must be estimated in order to incorporate the aero-propulsive interaction effects in the design process. This section proposes a method to estimate these terms for distributed propellers mounted ahead of the wing leading-edge.

1. Geometrical Description of the DP System

The geometrical layout of the system is shown in Fig. 4. This simplified representation assumes that the wing has a rectangular planform of span b and chord c , and that the propulsors are not located near the wing root or tip. The DP system is considered to be an array of N propulsors of diameter D_p ($N/2$ propulsors per semi-wing, where N is equal to N_1 or N_2 depending on whether the DP system corresponds to the primary or secondary powertrain, respectively), aligned in spanwise direction with a separation distance of $\Delta y D_p$. The propulsors are positioned at an angle α_p relative to the freestream velocity vector. For a given number of propulsors and fraction of wingspan occupied by the DP array (ΔY), the diameter of the propulsors can be computed as

$$D_p = \frac{\Delta Y}{N(1 + \Delta y)} b. \quad (21)$$

In Eq. 21, N and ΔY are selected as design variables, while the diameter of the propulsors is left as dependent variable. This approach is preferred since the span interval along which propulsors are installed can be limited by structural or geometrical constraints. Given that $b = \sqrt{SA}$ is an extensive parameter, and is therefore unknown in the sizing process, the propulsor diameter must be expressed in a normalized manner as

$$\frac{D_p^2}{W} = \frac{\Delta Y^2}{N^2 (1 + \Delta y)^2} \frac{A}{(W/S)}, \quad (22)$$

hereby defining a parameter which indicates how much propulsor-disk area is needed per unit of aircraft weight W , as a

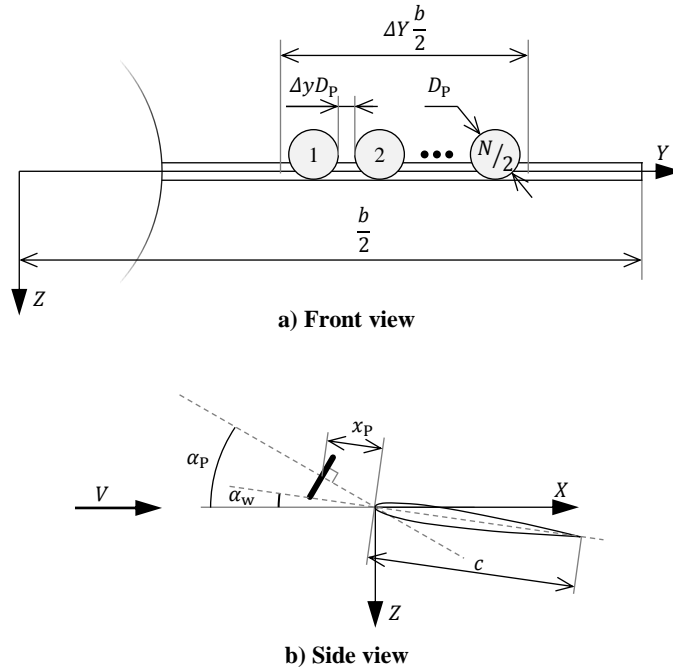


Fig. 4 Simplified DP-system representation, indicating the main geometrical parameters.

function of geometrical parameters and the wing loading of the aircraft. This parameter has units of m^2/N , and can therefore be interpreted as the inverse of a weight-oriented disk loading.

When selecting the geometrical design parameters of the DP system, it is important to verify that the total disk area is compatible with the propulsive efficiency assumed for each flight condition. While some authors argue that DP can improve propulsive efficiency through an increase in effective bypass ratio [4], this is not always the case: when the amount of space available to install the propulsors on an aircraft is finite, the total disk area tends to zero as $N \rightarrow \infty$. In other words, if a large number of propulsors is selected for a determined span interval and the required thrust-to-weight ratio is high, the thrust may be impossible to produce efficiently with the available disk area. Actuator disk theory shows that there is a maximum theoretical propulsive efficiency for a given thrust coefficient (see e.g. Ref. [47]), which can be translated into a maximum theoretical thrust coefficient $T_{c,\max}$ for an assumed propulsive efficiency:

$$T_{c,\max} = \frac{\pi}{8} \left[\left(\frac{2}{\eta_{\text{dp,isolated}}} - 1 \right)^2 - 1 \right]. \quad (23)$$

In Eq. 23, the thrust coefficient T_c of the DP propulsors can be expressed as a function of the required thrust-to-weight ratio and D_p^2/W using

$$T_c = \frac{1}{N} \frac{\chi(T/W)}{\rho V^2 (D_p^2/W)}. \quad (24)$$

The simplest way to verify that the thrust coefficient obtained at the design point does not exceed a maximum specified value $T_{c,\max}$ is to plot one constraint line $W_{\text{TO}}/P_p = f(W_{\text{TO}}/S, T_{c,\max})$ in the propulsive power-loading diagram for each performance constraint using Eq. 24. Contrary to the performance constraints, these additional constraints impose a lower bound on the feasible power-loading values. In this study, the design parameters and assumptions were verified to not violate these constraints, even though they are not explicitly plotted in the power-loading diagrams to improve their readability.

2. Estimation of ΔC_L and ΔC_D

Modeling the impact of tractor propellers on wing performance boils down to estimating the ‘‘Delta’’ terms of Eqs. 2, 3, and 4. Several assumptions are required in order to obtain a reasonable estimation with the information available in the preliminary sizing phase. Firstly, the propeller is modeled as an actuator disk in uniform axial inflow, and thus the upstream effect of the wing on the propeller is neglected ($\Delta\eta_{\text{dp}} = 0$). Secondly, the effect of each propeller on the adjacent ones is neglected. Thirdly, the wing is assumed to have a symmetric airfoil. Furthermore, the flow is attached, and the wing is fully immersed in the slipstream, i.e., half of the slipstream flows under the wing and half over the wing. And finally, the effect of the propellers on the wing is limited to the spanwise interval occupied by the disks (ΔY), and—within this spanwise interval—the effect on the wing is uniform in spanwise direction. Due to these

strong simplifications, the accuracy of this approach requires further investigation, especially in high-lift conditions. Nonetheless, its simplicity and sensitivity to top-level design parameters make it suitable for the preliminary sizing phase and useful to demonstrate the applicability of the proposed sizing method.

The first step is to compute the axial induction factor at the propeller disk (a_p) as a function of the propeller thrust coefficient, given by Eq. 24. From actuator disk theory it is known that

$$a_p = \frac{V_p - V}{V} = \frac{1}{2} \left(\sqrt{1 + \frac{8}{\pi} T_c} - 1 \right), \quad (25)$$

where $V_p - V$ is the velocity increase at the propeller disk. Due to contraction, the slipstream velocity impinging on the wing is higher than at the propeller disk. Following to the derivation of Veldhuis [47], the contraction ratio of the slipstream at the wing leading-edge (R_w/R_p) can be expressed as

$$\frac{R_w}{R_p} = \sqrt{\frac{1 + a_p}{1 + a_p \left(1 + \frac{x_p/R_p}{\sqrt{(x_p/R_p)^2 + 1}} \right)}}, \quad (26)$$

where x_p/R_p is the axial position of the propeller with respect to the wing leading edge, expressed as a fraction of its radius. From conservation of mass in incompressible flow it follows that

$$a_w = \frac{a_p + 1}{(R_w/R_p)^2} - 1. \quad (27)$$

With this, the velocity increase due to the thrust generated by the propellers at the wing leading-edge is known. Following the derivation of Patterson and German [48] and modifying their equation to remove the singularity at $c_l = 0$, one can compute the sectional lift coefficient increase as

$$\Delta c_l = 2\pi \left[(\sin \alpha_w - a_w \beta \sin(\alpha_p - \alpha_w)) \sqrt{(a_w \beta)^2 + 2a_w \beta \cos \alpha_p + 1} - \sin \alpha_w \right], \quad (28)$$

where α_w is the geometric angle of attack of the wing and β is a finite-slipstream correction factor. Since in the sizing process the angle of attack of the wing is unknown, it has to be estimated using the three-dimensional lift coefficient.

For this, the expression presented by Roskam [49] can be used:

$$\alpha_w \approx \frac{C_{L_{\text{airframe}}}}{2\pi A} \left[2 + \sqrt{A^2(1 - M^2) \left(1 + \frac{\tan^2 \Lambda_{c/2}}{1 - M^2} \right) + 4} \right]. \quad (29)$$

In Eq. 29, M is the freestream Mach number and $\Lambda_{c/2}$ the wing half-chord sweep angle. Since the aero-propulsive model assumes a rectangular wing, in this case the sweep angle is $\Lambda_{c/2} = 0$. With the aforementioned simplifications and assuming that $\Delta y \ll 1$, the sectional lift-coefficient increase obtained from Eq. 28 can be related to the wing

lift-coefficient increase through

$$\Delta C_L = \Delta c_l \cdot \Delta Y. \quad (30)$$

Determining the finite-slipstream correction factor β of Eq. 28 is a critical step in the process. If this term is neglected, the lift increase can be significantly over-estimated, especially for small ratios between the slipstream radius and wing chord [50]—as is the case for distributed propulsion. To this end, Patterson [29] generated a surrogate model based on CFD simulations of an actuator disk in front of a two-dimensional wing with a modified NACA 0012 airfoil. The surrogate model is used in this study to compute β as a function of a_P , x_P/c , and R_P/c . It is worth noting that this surrogate model uses the induced velocity far downstream of the disk as input, which according to actuator disk theory is equal to $(1 + 2a_P)V$. Furthermore, x_P/c can be related to x_P/R_P through the ratio between the propeller radius and the wing chord, which can be expressed as

$$\frac{R_P}{c} = \frac{1}{2} \sqrt{\left(\frac{D_P^2}{W}\right) \left(\frac{W}{S}\right) A}. \quad (31)$$

In order to evaluate the impact of the propeller on wing drag, several contributions have to be analyzed. Firstly, the increase in zero-lift drag is related to the increase in friction drag on the wing surface due to increased dynamic pressure in the slipstream. This contribution can be calculated using

$$\Delta C_{D_0} = \Delta Y a_w^2 c_f, \quad (32)$$

where c_f is the sectional skin friction coefficient, for which a typical value of 0.009 can be used [51]. Since at this stage of the design process not enough information is available to obtain a meaningful estimation of the change in wetted area when replacing one large nacelle by multiple smaller ones, this contribution to ΔC_{D_0} is neglected.

The increase in lift-induced drag can be attributed to an increase in C_L^2 on one hand, and to a change in the Oswald factor on the other. The former can be estimated by assuming a parabolic polar and expanding C_L^2 such that

$$\Delta C_{D_i} = \frac{\Delta C_L^2 + 2C_{L,\text{airframe}}\Delta C_L}{\pi A e}. \quad (33)$$

The change in Oswald factor due to aero-propulsive interaction, meanwhile, is assumed to be limited to a change in the span efficiency of the wing. However, the variation in span efficiency depends on a large number of design parameters and operating conditions, and is therefore difficult to estimate analytically. At high thrust settings, the increased velocity and swirl in the propeller slipstream lead to pronounced peaks in the spanwise loading distribution, decreasing the span efficiency. At low thrust settings, on the other hand, the trends are less clear. While some studies predict a decrease in span efficiency [29], others show an increase in span efficiency due to improved swirl recovery [52]. Since these effects

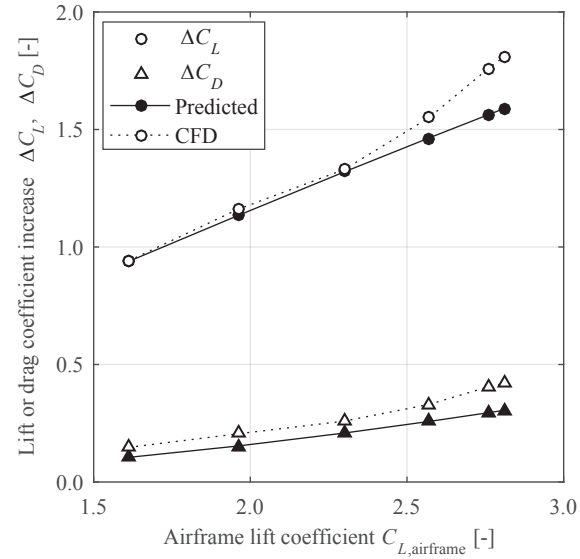
cannot be quantified with the information available in the preliminary sizing phase, the change in span efficiency is neglected. This simplification is more accurate for DP systems than for single-propeller systems, since the increase in lift is distributed along the span of the wing instead of being concentrated at a determined spanwise station.

3. Verification of the Aero-Propulsive Model

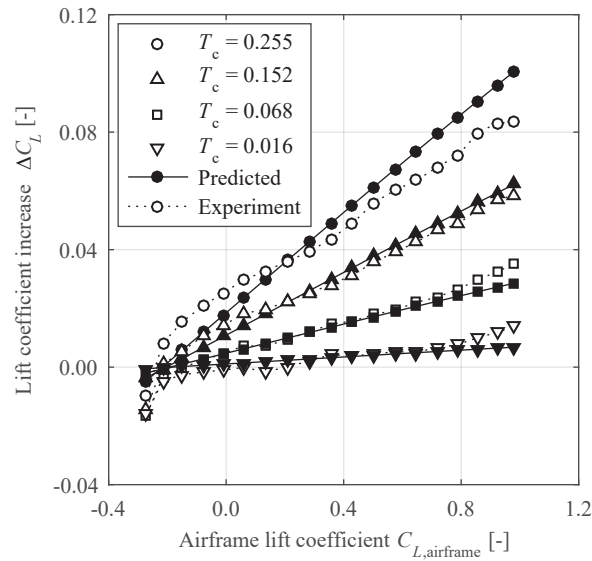
In order to verify that the simplified aero-propulsive model captures the ΔC_L and ΔC_D trends correctly, the model is evaluated for a range of airframe lift coefficients and compared to CFD simulations of the NASA X-57 demonstrator. The geometrical parameters, operating conditions, and results are based on the studies of Deere et al. [53]. The CFD simulations analyzed the high-aspect ratio wing ($A = 15$) with 12 propellers in approach conditions, with a flap deflection of 30° . For the comparison, an Oswald factor of $e = 0.8$ was selected based on work of Patterson [29], and a propeller angle of attack of $\alpha_P = 0^\circ$ was assumed. The changes in lift and drag coefficient predicted with the aero-propulsive model are presented in Fig. 5a along with the CFD results. The results agree well in terms of ΔC_L . A slight deviation is visible for high airframe lift coefficients ($C_{L,airframe} > 2.5$) as the maximum airframe lift coefficient of 2.7 is approached. Figure 5a also shows that the aero-propulsive model underestimates the increase in drag coefficient, which is expected since the impact of DP on the span efficiency is neglected[†]. Counterintuitively, for the aircraft considered in this study, this discrepancy leads to a conservative design. The main impact of DP on the aerodynamic performance of the aircraft is an increase in L/D due to increased wing loading, and not due to improved L/D for a given wing loading. The maximum wing loading is determined in landing conditions, for which a higher drag coefficient is beneficial since more thrust is required to maintain the same approach speed. This leads to an increase in ΔC_L , which in turn increases the maximum allowable wing loading.

The predictions are also compared to the experimental data of Sinnige et al. [52], to check whether the model is accurate for other propeller configurations. These experiments studied a single tractor propeller mounted on a low-aspect-ratio wing. The wing airfoil was cambered, and the performance was evaluated at low lift coefficients. Initial comparisons between the analytical model and experimental data showed that the model is not capable of directly capturing the performance trends. This is attributed to several reasons. Firstly, at low lift coefficients, the symmetric-airfoil assumption becomes less accurate: at $\alpha_P = 0^\circ$, $\alpha_w = 0^\circ$, a symmetric airfoil generates zero lift independently of thrust, while a cambered airfoil produces more lift as thrust is increased. Secondly, the diameter of the propeller was not small when compared to the span of the wing ($D_P/b = 0.32$). Therefore, the propeller has a relatively larger impact on the lift distribution outside the slipstream. Furthermore, the swirl in the slipstream has a larger impact on the spanwise lift distribution. A more detailed analysis showed that the trends could be estimated with reasonable accuracy if the effect of airfoil camber was represented by means of a small propeller incidence angle; in this case,

[†]Evaluation of the aero-propulsive model with an Oswald-factor penalty of -0.2 leads to a nearly perfect agreement between the predicted ΔC_D values and those obtained from CFD in Fig. 5. However, this arbitrary value would not be justifiable for other configurations or thrust coefficients.



a) Distributed propulsion ($T_c = 0.611$, $\alpha_p = 0^\circ$)



b) Single propeller ($\alpha_p = \alpha_w - 2^\circ$)

Fig. 5 Comparison of the aero-propulsive model with a) CFD simulations of the NASA X-57 wing [53] and b) experimental data of a single tractor propeller [52].

-2° with respect to the wing. The resulting ΔC_L curves[‡] are shown in Fig. 5b for four thrust coefficients. With this correction, the trends predicted by the model can be applied to the preliminary sizing process. Therefore, in summary, the verification procedure shows that the model is applicable to high-aspect-wings at high lift coefficients and with a large number of propellers, while it is not accurate for wings at low angles of attack and with large propellers, unless experimental or numerical data are available to correct the model for the setup considered.

[‡]Wing drag data were not representative for comparison, due to the effect of the slipstream on trailing-edge flow separation at low Reynolds numbers during the experimental campaign.

B. Top-Level Requirements and Assumptions

A regional transport aircraft comparable to the ATR 72-600 is considered, with a harmonic range of $R = 1528$ km (825 nautical miles) and a payload of 7500 kg. The aircraft has a cruise speed of $M_{cr} = 0.41$ at a cruise altitude of 5486 m (18,000 ft), and the approach speed must be no greater than 59 m/s (115 kts). In the case of a balked landing, the aircraft must be able to attain a climb gradient of 2.1% at 1.4 times the reference stall speed with one engine inoperative [54]. Furthermore, a diversion range of 370 km (200 nm) is required, for which a diversion altitude and Mach number of 3048 m (10,000 ft) and 0.3 are assumed, respectively. Finally, the aircraft must be able to take off with a field length of less than 1333 m. These aircraft requirements are collected in Table 2. The design parameters selected to meet these requirements are given in Table 3. Several of the values shown in these tables are based on ATR 72-600 reference data [55]. Three powertrain architectures are examined as candidates: a conventional turboprop, a serial powertrain with DP, and a partial-turboelectric (PTE) powertrain with DP.

Table 2 Top-level aircraft requirements.

Requirement	Value
Payload, M_{PL} [t]	7.5
Cruise altitude, h_{cr} [m]	5486
Cruise Mach number, M_{cr} [-]	0.41
Range, R [km]	1528
Approach speed [m/s]	59
OEI BL climb gradient [%]	2.1
OEI BL stall speed margin [-]	1.4
Diversion altitude [m]	3048
Diversion Mach number [-]	0.3
Diversion range [km]	370
Take-off field length [m]	1333

Table 3 Selected design parameter values.

Parameter	Value
Aspect ratio, A [-]	12
Half-chord sweep, $\Lambda_{c/2}$ [rad]	0
Taper ratio [-]	0.62
Root thickness-to-chord ratio [-]	0.18
N ^o of primary propulsors, N_1 [-]	2
N ^o of secondary propulsors, N_2 [-]	12
DP span fraction, ΔY [-]	0.6
Spacing between DP propulsors, Δy [-]	0.01
Axial position of DP propulsors, x_p/c [-]	0.2

Regarding the assumed aircraft properties, the parameters which depend on the aircraft configuration (clean, take-off, or landing) are shown in Table 4. These parameters are presented per performance constraint. For all three design

concepts, no thrust vectoring is considered, i.e. $\alpha_p = 0^\circ$. Furthermore, lower propulsive-efficiency values are assumed for the secondary propulsors of the serial architecture than for the PTE architecture. While the latter presents two propulsion systems, in the serial configuration all thrust has to be produced by the DP system. Consequently, it requires higher disk-loading values, and hence the propulsive efficiency must be lower in order to satisfy the maximum thrust-coefficient constraint (Eq. 24).

Table 4 Assumed aerodynamic and mission properties per constraint. All parameters are non-dimensional.

	Cruise speed	Approach speed	Take-off distance	OEI climb gradient
Flap configuration	clean	landing	take-off	landing
Landing gear position	retracted	extended	extended	retracted
Zero-lift drag coefficient, C_{D_0}	0.022	0.087	0.037	0.067
Oswald factor, e	0.8	0.95	0.9	0.95
Maximum lift coefficient, $C_{L_{\max, \text{airframe}}}$	-	2.7	2.1	2.7
Prop. efficiency (primary), η_{p1}	0.85	0.8	0.75	0.8
Prop. efficiency (secondary, serial), η_{p2}	0.8	0.6	0.7	0.7
Prop. efficiency (secondary, PTE), η_{p2}	0.85	0.65	0.75	0.8
Aircraft weight fraction, f_W	0.98	0.95	1	0.95
Gas turbine throttle, ξ_{GT}	0.8	0.5	1	1
Supplied power ratio (serial), Φ	0.05	0	0.1	0.1
Shaft power ratio (PTE), φ	0.1	0.8	0.4	0.4

Additionally, several assumptions related to the hybrid-electric powertrain are gathered in Table 5. The weights of the gearbox, PMAD and propulsors are neglected. The efficiency and specific power of the electrical machines are based on the technology goals presented by Jansen et al. [9], and include both the electrical machine itself and the associated inverter or rectifier. For the batteries, a specific energy of 500 Wh/kg at pack level is selected, which is considered an optimistic value for the 2035 time frame, close to the theoretical limits of lithium-ion batteries at cell level [12, 56, 57]. Moreover, a specific power of 1 kW/kg is assumed at pack level.

Table 5 Assumed HEP component technology levels.

Parameter	Value
Battery pack specific energy, e_{bat} [Wh/kg]	500
Battery pack specific power [kW/kg]	1
Minimum SOC [%]	20
EM specific power [kW/kg]	7.7
EM efficiency (η_{EM1} or η_{EM2}) [-]	0.96
PMAD efficiency, η_{PM} [-]	0.99
Gearbox efficiency, η_{GB} [-]	0.96
Gas turbine efficiency, η_{GT} [-]	0.3

C. Power-Control Strategies

The designer must specify the values of the power-control parameters defined in Sec. II.B.2 for each performance constraint and mission segment included in the sizing process. For conventional aircraft, this is limited to the gas-turbine throttle. However, for hybrid-electric aircraft, up to two additional design parameters (Φ and φ) have to be specified per constraint and mission segment. For this demonstration case, a simplified mission profile is assumed which includes the climb, cruise, and descent phases for both the nominal mission and a diversion. The take-off and landing segments are neglected in the mission analysis, although their power requirements are included in the power-loading diagrams. During climb and descent, all power-control parameters are specified as input, while during cruise, the flight condition is completely specified in terms of speed and altitude, and thus one control parameter is a dependent variable. Note that consistent power-control values must be used if the power requirements of a determined mission segment appear as a performance constraint in the power-loading diagrams, such as a cruise-speed constraint.

In this study, the power-control strategy is selected based on a series of qualitative arguments, although a systematic optimization study could have a large impact on the resulting design [24]. The values of ξ_{GT} , Φ , and φ used for each performance constraint can be found in Table 3. The power-control profiles chosen for the mission analysis are shown for the three designs with thin lines in Fig. 6. In this example, ξ_{GT} , Φ , and φ are assumed to vary linearly with altitude during climb and descent, and to vary linearly with range during cruise. The thick lines are a result of applying the point model for a fixed flight condition during the mission analysis and are therefore not known a priori, although they have been included here for completeness. Note that the throttle values obtained during cruise do not necessarily coincide with the values specified in Table 3, since the cruise-speed constraint may not be actively limiting the installed power of the powertrain components (see Sec. III.D). Only the climb, cruise and descent phases of the nominal mission are included in Fig. 6. Similar control strategies are applied for the diversion phase, though with reduced throttle to compensate the decrease in aircraft weight.

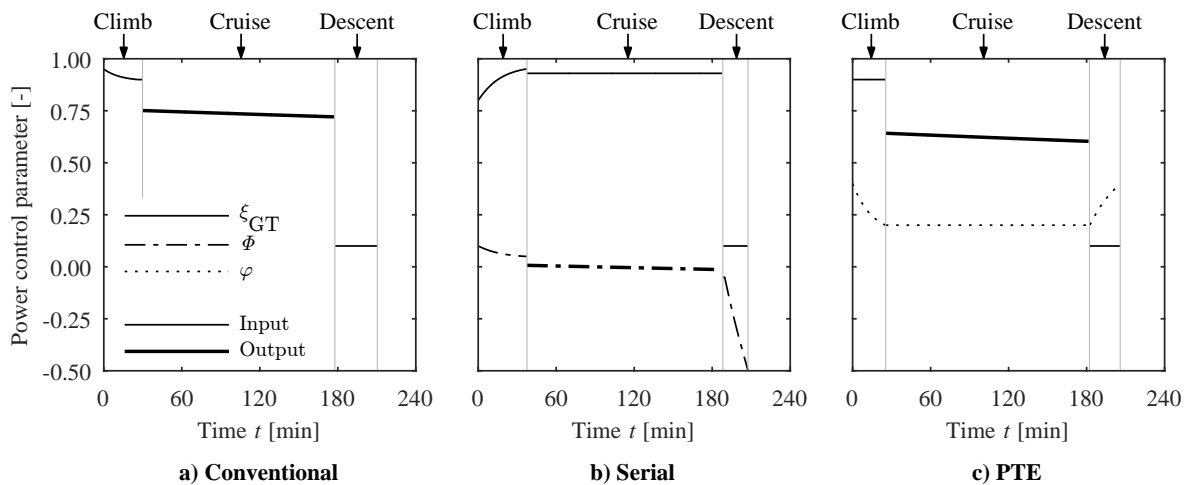


Fig. 6 Power-control profiles throughout the nominal mission of the three powertrain architectures.

For the conventional architecture (Fig. 6a), the throttle values are specified as input during climb and descent, with the cruise throttle decreasing over time to compensate the reduction in aircraft weight. For the serial architecture (Fig. 6b), throttle is specified during cruise, while the supplied power ratio is adapted to compensate the changes in thrust requirements. Consequently, the gas turbine operates near its sizing condition for a large part of the mission. This can improve its efficiency [40, 58], although sensitivity to this benefit has not been included here. During descent, a negative supplied power ratio is specified, such that the power produced by the gas turbine in idle conditions is used to recharge the batteries. This extra battery energy can be used for the diversion phase, or to reduce charging time on the ground.

Finally, for the PTE architecture (Fig. 6c), a φ profile is specified throughout the mission in order to maximize aero-propulsive performance, while the throttle is varied accordingly. The control strategy was selected as follows. During take-off, the power is shared equally between the primary and secondary propulsors (see Table 4). This spreads the loads over a larger area for a given primary-propulsor size, or reduces its size for a given disk loading. The first option would increase propulsive efficiency with respect to a conventional configuration, while the second would entail secondary benefits such as reduced landing gear length, both of which are only quantified in later stages of the design process. During cruise, low φ values are used since the distributed propellers decrease the lift-to-drag ratio of the wing in this flight condition. This does not, however, imply that the aircraft would present a lower L/D than the conventional configuration if φ were increased: the use of DP in low-speed conditions can increase the maximum wing loading (see Sec. III.D.2), which in turn increases the lift-to-drag ratio. Finally, during approach, the gas turbine throttle is reduced but most power is diverted to the DP system, thus enhancing lift and increasing the maximum wing-loading. These relations between the power-control strategy and the aero-propulsive effects highlight the importance of understanding and incorporating both aspects early in the design process.

D. Results

1. Comparison to Reference Data

In this section the results of the conventional configuration are compared to reference data of the ATR 72-600 at maximum payload [55], in order to verify that the preliminary sizing method was correctly formulated and implemented. Since the approach described in Sec. II contains only simplified physics-based derivations, the accuracy of the method for hybrid-electric concepts will depend largely on the accuracy of the aero-propulsive model, assumed component efficiencies, and weight correlations.

Table 6 presents the traditional Class-I results of the conventional configuration and reference aircraft. The TOM is underestimated by 3.8%, mainly due to an underestimation of the operative empty mass (OEM), which is calculated using the Class-I empirical correlation of Raymer [32]. The fuel mass, on the other hand, is slightly over-estimated, indicating that the assumed aerodynamic properties and component efficiencies may differ from the reference aircraft. Nonetheless, the deviations are within the accuracy expected from a preliminary sizing method, and therefore the method is deemed applicable for comparing different propulsion-system architectures under equal assumptions.

Table 6 Comparison between a reference ATR 72-600 and the results obtained for the conventional configuration.

	Reference [§]	Conv.	Difference
m_{TO} [t]	22.8	21.9	-3.8%
m_{OE} [t]	13.3	12.3	-7.4%
m_f [t]	2.0	2.1	+6.6%
W_{TO}/S [kN/m ²]	3.67	3.60	-1.8%
$W_{TO}/P_{GT,max,SLS}$ [N/W]	0.058	0.055	-5.2%

2. Design Wing Loading and Power Loading

The power-loading diagrams obtained for the three different powertrain architectures are shown in Fig. 7. Only the most instructive component diagrams are included for brevity, although in practice one diagram exists per component included in the powertrain model. In these diagrams, the feasible design space, shaded in gray, represents the combinations of wing loading and power loading which generate an aircraft capable of satisfying all performance requirements. The designer must analyze these diagrams and select the aircraft's wing-loading. Then, for each component, a power-loading value must be selected. Generally, the maximum power-loading allowed at the chosen wing-loading is selected for each component, since this leads to a minimum component weight. The diagrams also show which performance requirement is actively constraining the maximum allowable power-loading of each component. This maximum power loading can be varied by, for example, changing the power-control variables of the limiting constraint.

Figure 7 clearly shows an increase in maximum wing loading due to DP. For the conventional architecture, no aero-propulsive effects have been included. In this way, the diagram of Fig. 7a can be compared with the reference aircraft, and the effect of including the aero-propulsive interaction in the sizing process can be distinguished. However, in practice, this configuration also presents appreciable interaction effects between the propeller and the wing. Thus, the actual increase in wing loading due to DP is slightly lower than suggested by Fig. 7. The increase in wing loading is higher for the serial architecture than for the PTE architecture, since for the latter the shaft power ratio is $\varphi = 0.8$ in landing conditions (see Table 4), and thus not all the power is used to enhance lift. For the PTE architecture, a shaft power ratio lower than unity was selected in landing conditions because, for the aerodynamic characteristics assumed, using all thrust to enhance lift in landing conditions leads to an excessively high wing-loading, with a negative impact on cruise performance. In practice this would imply that a smaller, less complex high-lift system could be used during landing, compensating the decrease in $C_{L,max,airframe}$ by increasing the shaft power ratio.

Several possible design points are included in Fig. 7. These show how the optimum design point in terms of one component generally does not coincide with the optimum size of other components. In this paper, the design point for maximum wing loading is selected, which for conventional aircraft often corresponds to the smallest wing size. However,

[§]Since the reference data provides P_{s1} instead of P_{gt} , the reference power-loading has been multiplied by η_{GB} in order to compare $W_{TO}/P_{GT,max,SLS}$ in equal conditions.

due to the large impact of the powertrain on TOM, for HEP aircraft it may be more beneficial to select a different design point, as demonstrated in the work of Finger et al. [27]. At the design point corresponding to maximum wing loading, all components in Fig. 7 are sized by the take-off constraint, except for the gas turbine of the serial architecture, which is

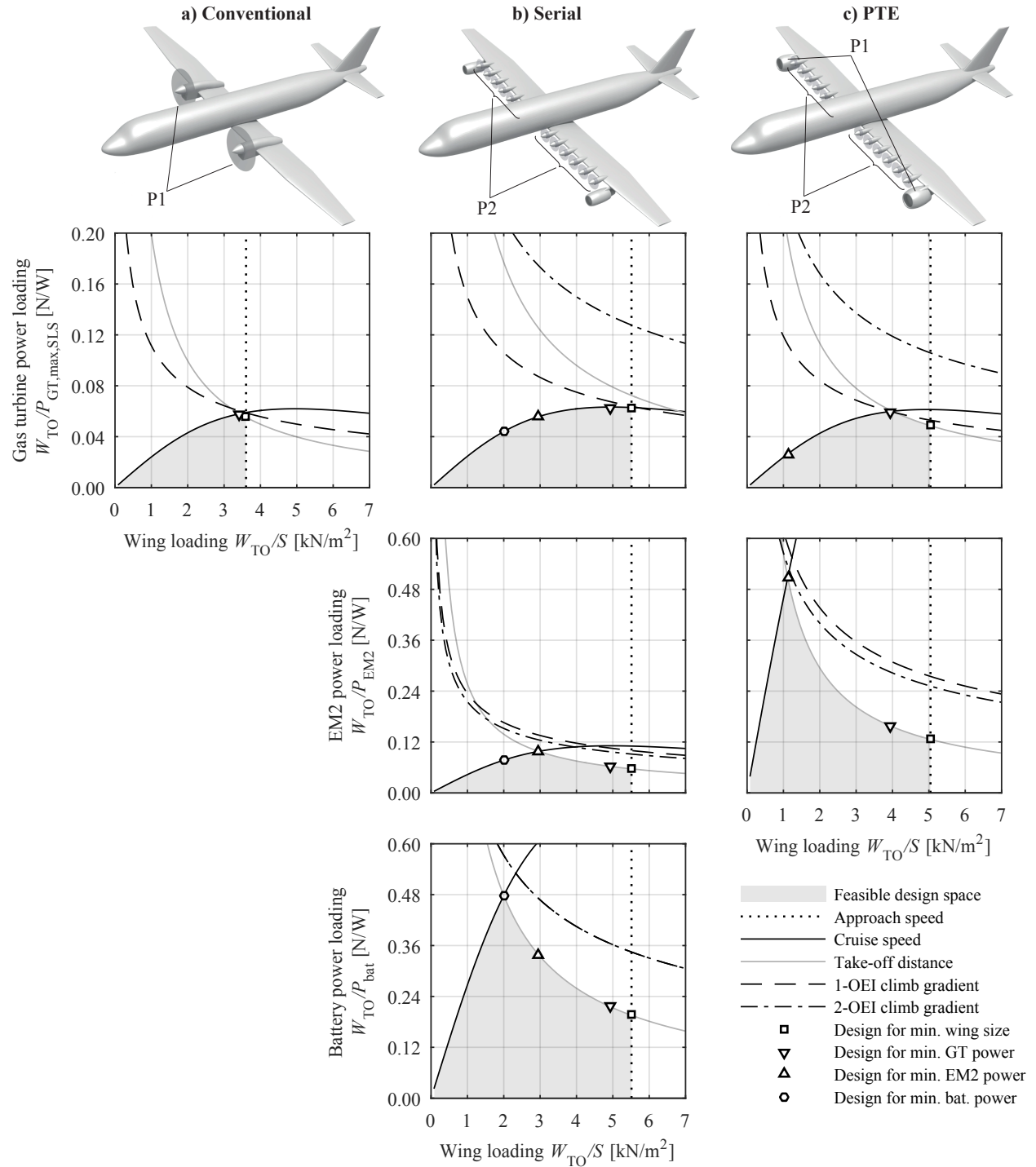


Fig. 7 Component power-loading diagrams for the (a) conventional, (b) serial, and (c) PTE powertrain architectures, including a notional representation of the propulsion system layout at the top.

sized by the cruise constraint. This is a result of the battery-assisted take-off. In all three cases, the OEI balked landing constraint is inactive but close to the design point of the gas turbine. The secondary electrical machines, on the other hand, can easily satisfy the OEI constraint. This highlights the benefit of having redundant propulsors in DP systems: while a failure in the primary powertrain branch requires the components of that branch to be over-sized by a factor 2, a failure in the secondary powertrain branch only requires the corresponding components to be over-sized by a factor 12/11. Moreover, when comparing the serial and PTE architectures, one can observe that a higher electrical-machine power-loading is achieved for the latter, since during take-off part of the propulsive power is generated by the primary propulsors. In any case, the highest power-loading values are obtained in the battery power-loading diagram of Fig. 7b. Given the sensitivity of TOM to battery energy and power requirements [10, 12, 20, 22], higher battery power-loading values are required to avoid an excessively high TOM.

3. Weight Breakdown and Energy Consumption

Table 7 collects the main results of the three designs. The table includes the payload-range energy efficiency as an overall aircraft performance metric [59], defined as

$$\text{PREE} = \frac{W_{\text{PL}}R}{E_{\text{miss}}}. \quad (34)$$

This non-dimensional parameter represents the amount of useful work, interpreted as the work required to transport a unit of payload weight over a unit of distance, is extracted per joule of energy consumed. Despite the higher wing-loading values obtained for the two HEP concepts, the serial configuration is 26% heavier than the conventional configuration, while the PTE configuration is 2% heavier. Nonetheless, the increased wing loading leads to a reduced wing area for both the serial (−18%) and PTE (−27%) configurations. The corresponding L/D increase is not large enough to offset the increase in aircraft weight, leading to increased energy consumption with respect to the conventional concept. This directly translates into a reduction in PREE, which is 28% and 3% lower for the serial and PTE configurations, respectively. The cruise lift-to-drag ratio of the PTE architecture is slightly higher than for the serial configuration, even though the latter presents a higher wing-loading. This is because, for the serial architecture, the lift coefficient during cruise is too high, exceeding the value corresponding to optimum L/D .

The differences in TOM of the three concepts are further clarified in the breakdowns presented in Fig. 8. The wing mass fraction is lower for the two HEP concepts, due to the increased wing loading. Figure 8 also shows that not only the fuel mass, but also the fuel fraction is slightly higher for the serial architecture than for the conventional concept. This indicates that, for the given mission, the increase in L/D does not offset the lower propulsive efficiency assumed for the DP system (see Table 4) and the power lost in the conversion from mechanical energy to electrical energy and vice versa. Figure 8 also shows that the total powertrain weight fractions of the serial (13%) and PTE (8%) architectures

Table 7 Summary of results obtained for the three architectures evaluated. Lift-to-drag ratio is presented as the average of the cruise phase.

	Conv.	Serial	PTE
m_{TO} [t]	21.9	27.7	22.4
W_{TO}/S [kN/m ²]	3.60	5.51	5.04
$W_{TO}/P_{GT,max,SLS}$ [N/W]	0.055	0.063	0.049
S [m ²]	60	49	44
$E_{f,miss}$ [GJ]	73.8	103.0	75.8
$E_{bat,miss}$ [GJ]	0	1.7	0
$(L/D)_{cr}$ [-]	17.5	18.4	18.5
PREE [-]	1.52	1.09	1.48

exceed the weight fraction of the conventional one (5%). Although in the serial architecture the gas-turbine weight fraction is reduced, this does not compensate the increase in weight due to the electrical components. The reduction in gas-turbine weight fraction is a consequence of the increased gas-turbine power-loading at the design point. This increase in power-loading is attributed to increased wing-loading due to aero-propulsive effects on one hand, and to the addition of battery power during take-off on the other. However, since all power has to be transmitted through the electrical components, the weight of the electrical machines is substantially higher than for the PTE architecture. Finally, even though Table 7 shows that the battery accounts for just 1.6% of the total energy consumed by the serial architecture during the nominal mission, it represents 5% of the total aircraft weight, thus having a substantial impact on TOM.

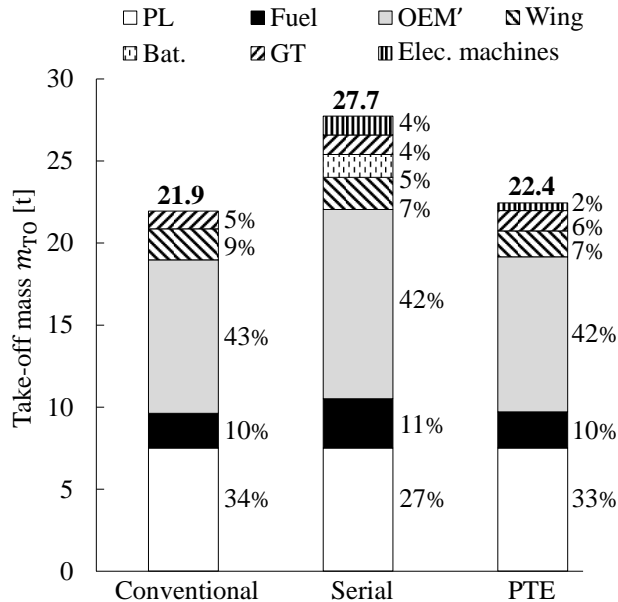


Fig. 8 Mass breakdown of the three configurations evaluated. Values are expressed in metric tons and as a percentage of take-off mass.

4. Analysis of Findings & Discussion

The results indicate that the two HEP concepts present no benefit with respect to a conventional powertrain. This is in line with the findings of previous studies, which show that either more optimistic e_{bat} values [9, 12, 22, 44] or reduced ranges [8, 17–19, 25] are required for the HEP concepts to be competitive. However, the results obtained in this study are conservative for several reasons. Firstly, the wing area of the HEP concepts was reduced at constant aspect ratio, instead of at constant span. If the latter approach had been taken, the lift-to-drag benefit due to DP would further increase. Secondly, the wing-loading increase enabled by DP would improve the short take-off and landing (STOL) capabilities of the aircraft, without significantly penalizing cruise performance. Thirdly, the potential increase in propulsive efficiency due to reduced disk loading has not been included in this demonstration case. Moreover, these results have been obtained for range, altitude, and Mach numbers for which the reference aircraft is optimized, without carrying out any systematic sensitivity or optimization studies for the hybrid-electric concepts. For example, for the assumed mission, the PTE concept consumes approximately 3% more energy than the conventional one, but presents a 6% higher lift-to-drag ratio. This indicates that this hybrid-electric concept is likely to be advantageous for longer ranges, such that the benefit in aero-propulsive efficiency can lead to a fuel weight reduction which offsets the powertrain weight penalty. For the serial configuration, on the other hand, no significant benefits are expected. Apart from the detrimental effect of batteries on aircraft weight, there are two additional reasons for this. Firstly, since all power has to be diverted to the secondary propulsors during take-off, the weight of the electrical machines is much higher than for the PTE configuration. Secondly, since the disk loading is higher for the serial configuration, lower propulsive efficiencies are achievable. Thus, powertrain layouts with two propulsion systems should not be discarded a priori due to their complexity or weight penalty, since they can be used in a much more beneficial manner throughout the mission.

Additional work is required to verify these claims. For this, propulsion systems which enhance cruise performance—such as tip-mounted propulsion, over-the-wing propulsion, or boundary-layer ingestion—should be analyzed in more depth. The proposed method is capable of performing such studies systematically if the corresponding aero-propulsive models are incorporated. Furthermore, it can be used in sensitivity or optimization studies to determine more optimal mission and power-control profiles, as well as to rapidly evaluate different combinations of mission requirements, powertrain architectures, and technology-level assumptions. The results of this study also provide valuable insight into possible areas of improvement. For example, the power-loading diagrams show which performance requirements are constraining for each component of each powertrain architecture, clearly indicating in which flight condition the aerodynamic or operational characteristics must be improved in order to obtain a benefit at aircraft level. In this sense, the method can be used as a first approach to relate the findings of detailed aero-propulsive studies to their impact at aircraft level.

IV. Conclusions

The preliminary sizing method described in this article can be used to determine the wing area, take-off weight, and installed power of the main powertrain components of conventional, hybrid-electric, and fully-electric fixed-wing aircraft. To this end, a simplified powertrain model is proposed, and a method to estimate the aero-propulsive interaction effects for leading-edge-mounted distributed-propulsion systems is presented. These models are subsequently applied to a regional transport aircraft. This demonstration case illustrates the additional design variables that must be specified by the designer when sizing a hybrid-electric aircraft, and shows how the component-oriented power-loading diagrams must be interpreted. The results indicate that, for the assumed technology levels and mission requirements, the use of leading-edge distributed-propulsion does not lead to any benefit at aircraft level when compared to a conventional powertrain. The aircraft concept featuring a partial turboelectric architecture consumes 3% more energy than a conventional configuration, while the concept featuring a serial powertrain architecture consumes 40% more energy. However, these values have been obtained without any systematic design-space-exploration or optimization studies. Moreover, the trends in wing loading and lift-to-drag ratio suggest that the proposed configuration can be competitive for other mission requirements, and that hybrid-electric propulsion can lead to a benefit at aircraft level if novel propulsion systems are carefully studied and integrated.

The method is flexible and sensitive to the relevant top-level design parameters, and can therefore be easily applied to evaluate a wide range of configurations and requirements. Moreover, it provides a quick and visually-evident way of relating the findings of higher-fidelity propulsion-system studies to their impact at aircraft level. Nevertheless, although the method constitutes a solid basis for more elaborate conceptual-design frameworks, multiple improvements can be incorporated to increase its accuracy. Most importantly, the powertrain model can be improved by, for example, incorporating the effect of battery state-of-charge, variable gas-turbine efficiency, and the thermal management system. Furthermore, additional aero-propulsive models should be developed for highly-integrated propulsion systems such as leading-edge distributed-propulsion, over-the-wing distributed-propulsion, tip-mounted propulsion, or boundary-layer ingestion, based on detailed aerodynamic studies. The implementation of different aero-propulsive models will broaden the applicability of the method and enable the rapid design-space exploration of a wide range of aircraft configurations.

Acknowledgments

This research was funded by the European Union's Horizon 2020 Clean Sky 2 Large Passenger Aircraft (LPA) program (CS2-LPA-GAM-2014-2015-01). The authors would like to thank the other partners of LPA WP1.6 and the NOVAIR project participants for their valuable feedback. Wing, tail, and fuselage CAD geometries were created based on reference aircraft data using Pacelab APD 6.0.

References

- [1] Bonet, J. T., Schellenger, H. G., Rawdon, B. K., Elmer, K. R., Wakayama, S. R., Brown, D. L., and Guo, Y., "Environmentally Responsible Aviation (ERA) Project - N+2 Advanced Vehicle Concepts Study and Conceptual Design of Subscale Test Vehicle (STV): Final Report," Technical Report NASA/CR-2011-216519, December 2011.
- [2] Advisory Council for Aviation Research and Innovation in Europe (ACARE), "Realising Europe's vision for aviation: Strategic research & innovation agenda, Vol. 1," Advisory Council for Aviation Research and Innovation in Europe, 2012.
- [3] Borer, N. K., Patterson, M. D., Viken, J. K., Moore, M. D., Clarke, S., Redifer, M. E., Christie, R. J., Stoll, A. M., Dubois, A., Bevirt, J. B., Gibson, A. R., Foster, T. J., and Osterkamp, P. G., "Design and Performance of the NASA SCEPTOR Distributed Electric Propulsion Flight Demonstrator," 16th AIAA Aviation Technology, Integration, and Operations Conference, Washington, DC, USA, June 13-17 2016. doi:10.2514/6.2016-3920.
- [4] Felder, J. L., Kim, H. D., and Brown, G. V., "Turboelectric Distributed Propulsion Engine Cycle Analysis for Hybrid-Wing-Body Aircraft," 47th AIAA Aerospace Sciences Meeting, Orlando, FL, USA, January 5-8 2009. doi:10.2514/6.2009-1132.
- [5] Rothaar, P. M., Murphy, P. C., Bacon, B. J., Gregory, I. M., Grauer, J. A., Busan, R. C., and Croom, M. A., "NASA langley distributed propulsion VTOL tilt-wing aircraft testing, modeling, simulation, control, and flight test development," 14th AIAA Aviation Technology, Integration, and Operations Conference, Atlanta, GA, USA, June 16-20 2014. doi:10.2514/6.2014-2999.
- [6] Schiltgen, B., Freeman, J. L., and Hall, D. W., "Aeropropulsive Interaction and Thermal System Integration within the ECO-150: A Turboelectric Distributed Propulsion Airliner with Conventional Electric Machines," 16th AIAA Aviation Technology, Integration and Operations Conference, Washington, DC, USA, June 13-17 2016. doi:10.2514/6.2016-4064.
- [7] Hermetz, J., Ridel, M., and Döll, C., "Distributed electric propulsion for small business aircraft: A concept-plane for key-technologies investigations," 30th Congress of the International Council of the Aeronautical Sciences, Daejeon, South Korea, 2016.
- [8] Stoll, A. M., and Mikić, G. V., "Design Studies of Thin-Haul Commuter Aircraft with Distributed Electric Propulsion," 16th AIAA Aviation Technology, Integration, and Operations Conference, Washington, DC, USA, June 13-17 2016. doi:10.2514/6.2016-3765.
- [9] Jansen, R. H., Bowman, C., Jankovsky, A., Dyson, R., and Felder, J., "Overview of NASA Electrified Aircraft Propulsion Research for Large Subsonic Transports," 53rd AIAA/SAE/ASEE Joint Propulsion Conference, Atlanta, GA, USA, July 10-12 2017. doi:10.2514/6.2017-4701.
- [10] Sgueglia, A., Schmollgruber, P., Bartoli, N., Atinault, O., Benard, E., and Morlier, J., "Exploration and Sizing of a Large Passenger Aircraft with Distributed Ducted Electric Fans," 2018 AIAA Aerospace Sciences Meeting, Kissimmee, FL, USA, January 8-12 2018. doi:10.2514/6.2018-1745.

- [11] Steiner, H. J., Seitz, A., Wieczorek, K., Plötner, K., Iskiveren, A. T., and Hornung, M., “Multi-disciplinary design and feasibility study of distributed propulsion systems,” 28th Congress of the International Council of the Aeronautical Sciences, Brisbane, Australia, September 23-28 2012.
- [12] Voskuijl, M., van Bogaert, J., and Rao, A. G., “Analysis and design of hybrid electric regional turboprop aircraft,” *CEAS Aeronautical Journal*, Vol. 9, 2018, pp. 15–25. doi:10.1007/s13272-017-0272-1.
- [13] Schmollgruber, P., Döll, C., Hermetz, J., Liaboeuf, R., Ridet, M., Cafarelli, I., Atinault, O., François, C., and Paluch, B., “Multidisciplinary Exploration of DRAGON: an ONERA Hybrid Electric Distributed Propulsion Concept,” 2019 AIAA Aerospace Sciences Meeting, San Diego, CA, USA, January 7-11 2019. doi:10.2514/6.2019-1585.
- [14] Gohardani, A. S., Doulergis, G., and Singh, R., “Challenges of future aircraft propulsion: A review of distributed propulsion technology and its potential application for the all electric commercial aircraft,” *Progress in Aerospace Sciences*, Vol. 47, 2011, pp. 369–391. doi:10.1016/j.paerosci.2010.09.001.
- [15] Kim, H. D., “Distributed Propulsion Vehicles,” 27th Congress of the International Council of the Aeronautical Sciences, Nice, France, September 19-24 2010.
- [16] Kim, J. H., Kwon, K. S., Roy, S., Garcia, E., and Marvis, D., “Megawatt-class Turboelectric Distributed Propulsion, Power, and Thermal Systems for Aircraft,” 2018 AIAA Aerospace Sciences Meeting, Kissimmee, FL, USA, January 8-12 2018. doi:10.2514/6.2018-2024.
- [17] Antcliff, K. R., and Capristan, F. M., “Conceptual Design of the Parallel Electric-Gas Architecture with Synergistic Utilization Scheme (PEGASUS) Concept,” 17th AIAA/ISSMO Multidisciplinary Analysis and Optimization Conference, Denver, CO, USA, June 5-9 2017. doi:10.2514/6.2017-4001.
- [18] Wroblewski, G. E., and Ansell, P. J., “Mission Analysis and Emissions for Conventional and Hybrid-Electric Commercial Transport Aircraft,” 2018 AIAA Aerospace Sciences Meeting, Kissimmee, FL, USA, January 8-12 2018. doi:10.2514/6.2018-2028.
- [19] Dean, T. S., Wroblewski, G. E., and Ansell, P. J., “Mission Analysis and Component-Level Sensitivity Study of Hybrid-Electric General Aviation Propulsion Systems,” 2018 AIAA Aerospace Sciences Meeting, Kissimmee, FL, USA, January 8-12 2018. doi:10.2514/6.2018-1749.
- [20] Cinar, G., Mavris, D. N., Emeneth, M., Schneegans, A., Riediger, C., Fefermann, Y., and Isikveren, A. T., “Sizing, Integration and Performance Evaluation of Hybrid Electric Propulsion Subsystem Architectures,” 55th AIAA Aerospace Sciences Meeting, Grapevine, TX, USA, January 9-13 2017. doi:10.2514/6.2017-1183.
- [21] Isikveren, A. T., Kaiser, S., Pornet, C., and Vratny, P. C., “Pre-design strategies and sizing techniques for dual-energy aircraft,” *Aircraft Engineering and Aerospace Technology: An International Journal*, Vol. 86(6), 2014, pp. 525–542. doi:10.1108/AEAT-08-2014-0122.

- [22] Pernet, C., and Isikveren, A. T., “Conceptual design of hybrid-electric transport aircraft,” *Progress in Aerospace Sciences*, Vol. 79, 2015, pp. 114–135. doi:10.1016/j.paerosci.2015.09.002.
- [23] Nam, T., Soban, D. S., and Mavris, D. N., “Power Based Sizing Method for Aircraft Consuming Unconventional Energy,” 43rd AIAA Aerospace Sciences Meeting and Exhibit, Reno, NV, USA, January 10-13 2005. doi:10.2514/6.2005-818.
- [24] Perullo, C., and Mavris, D., “A review of hybrid-electric energy management and its inclusion in vehicle sizing,” *Aircraft Engineering and Aerospace Technology: An International Journal*, Vol. 86(6), 2014, pp. 550–557. doi:10.1108/AEAT-04-2014-0041.
- [25] Kreimeier, M., and Stumpf, E., “Benefit evaluation of hybrid electric propulsion concepts for CS-23 aircraft,” *CEAS Aeronautical Journal*, Vol. 8, 2017, pp. 691–704. doi:10.1007/s13272-017-0269-9.
- [26] Kruger, M., Byahut, S., Uranga, A., Dowdle, A., Gonzalez, J., and Hall, D. K., “Electrified Aircraft Trade-Space Exploration,” 2018 Aviation Technology, Integration, and Operations Conference, Atlanta, GA, USA, June 25-29 2018. doi:10.2514/6.2018-4227.
- [27] Finger, D. F., Braun, C., and Bil, C., “An Initial Sizing Methodology for Hybrid-Electric Light Aircraft,” 2018 Aviation Technology, Integration, and Operations Conference, Atlanta, GA, USA, June 25-29 2018. doi:10.2514/6.2018-4229.
- [28] Pernet, C., “Conceptual Design Methods for Sizing and Performance of Hybrid-Electric Transport Aircraft,” PhD Dissertation, Technical University of Munich, 2018.
- [29] Patterson, M. D., “Conceptual Design of High-Lift Propeller Systems for Small Electric Aircraft,” PhD Dissertation, Georgia Institute of Technology, 2016.
- [30] Torenbeek, E., *Synthesis of Subsonic Airplane Design*, Delft University Press, 1982.
- [31] Roskam, J., *Airplane Design*, DARcorporation, 1985.
- [32] Raymer, D. P., *Aircraft design: A conceptual approach*, AIAA Education Series, 2002. doi:10.2514/4.869112.
- [33] ESDU, “Thrust and drag accounting for propeller/airframe interaction,” ESDU 85017, 1985.
- [34] Smith Jr., L. H., “Wake Ingestion Propulsion Benefit,” *Journal of Propulsion and Power*, Vol. 9(1), 1993, pp. 74–83. doi:10.2514/3.11487.
- [35] Seitz, A., and Gologan, C., “Parametric design studies for propulsive fuselage aircraft concepts,” *CEAS Aeronautical Journal*, Vol. 6(1), 2015, pp. 69–82. doi:10.1007/s13272-014-0130-3.
- [36] Mikić, G. V., Stoll, A. M., Bevirt, J., Grah, R., and Moore, M. D., “Fuselage Boundary Layer Ingestion Propulsion Applied to a Thin Haul Commuter Aircraft for Optimal Efficiency,” 16th AIAA Aviation Technology, Integration, and Operations Conference, Washington, DC, USA, June 13-17 2016. doi:10.2514/6.2016-3764.

- [37] Drela, M., "Power Balance in Aerodynamic Flows," *AIAA Journal*, Vol. 47(7), 2009, pp. 1761–1771. doi:10.2514/1.42409.
- [38] Patterson, M. D., and Borer, N. B., "Approach Considerations in Aircraft with High-Lift Propeller Systems," 17th AIAA Aviation Technology, Integration, and Operations Conference, Denver, CO, USA, June 5-9 2017. doi:10.2514/6.2017-3782.
- [39] National Academies of Sciences, Engineering, and Medicine, *Commercial Aircraft Propulsion and Energy Systems Research: Reducing Global Carbon Emissions*, National Academies Press, 2016. doi:10.17226/23490.
- [40] Ang, A. W. X., Gangoli Rao, A., Kanakis, T., and Lammen, W., "Performance analysis of an electrically assisted propulsion system for a short-range civil aircraft," *Proceedings of the Institution of Mechanical Engineers, Part G: Journal of Aerospace Engineering*, 2018. doi:10.1177/0954410017754146.
- [41] Ruijgrok, G. J. J., *Elements of airplane performance*, Delft University Press, 1996.
- [42] Marwa, M., Martin, S. M., Martos, B. C., and Anderson, R. P., "Analytic and Numeric Forms for the Performance of Propeller-Powered Electric and Hybrid Aircraft," 55th AIAA Aerospace Sciences Meeting, Grapevine, TX, USA, January 9-13 2017. doi:10.2514/6.2017-0211.
- [43] Jagannath, R., Bane, S. P. M., Nalim, M. R., and Javed Khan, M., "A Simplified Method To Calculate The Fuel Burn Of A Hybrid-Electric Airplane," 50th AIAA/ASME/SAE/ASEE Joint Propulsion Conference, Cleveland, OH, USA, July 28-30 2014. doi:10.2514/6.2014-3490.
- [44] Isikveren, A. T., Pornet, C., Vratny, P. C., and Schmidt, M., "Optimization of Commercial Aircraft Using Battery-Based Voltaic-Joule/Brayton Propulsion," *Journal of Aircraft*, Vol. 54(1), 2017, pp. 246–261. doi:10.2514/1.C033885.
- [45] Seitz, A., Bijewitz, J., Kaiser, S., and Wortmann, G., "Conceptual investigation of a propulsive fuselage aircraft layout," *Aircraft Engineering and Aerospace Technology: An International Journal*, Vol. 86(6), 2014, pp. 464–472. doi:10.1108/AEAT-06-2014-0079.
- [46] Vratny, P. C., Gologan, C., Pornet, C., Isikveren, A. T., and Hornung, M., "Battery Pack Modeling Methods for Universally-Electric Aircraft," 4th CEAS Air & Space Conference, Linköping, Sweden, September 16-19 2013.
- [47] Veldhuis, L. L. M., "Propeller Wing Aerodynamic Interference," PhD Dissertation, Delft University of Technology, 2005.
- [48] Patterson, M. D., and German, B. J., "Simplified Aerodynamics Models to Predict the Effects of Upstream Propellers on Wing Lift," 53rd AIAA Aerospace Sciences Meeting, Kissimmee, FL, USA, January 5-9 2015. doi:10.2514/6.2015-1673.
- [49] Roskam, J., *Methods for estimating drag polars of subsonic airplanes*, Roskam Aviation and Engineering Corporation, 1971.
- [50] Ting, L., Liu, C. H., and Kleinstein, G., "Interference of Wing and Multipropellers," *AIAA Journal*, Vol. 10(7), 1972, pp. 906–914. doi:10.2514/3.50244.
- [51] Biber, K., "Estimating Propeller Slipstream Drag on Airplane Performance," *Journal of Aircraft*, Vol. 48(6), 2011, pp. 2172–2174. doi:10.2514/1.C031458.

- [52] Sinnige, T., van Arnhem, N., Stokkermans, T. C. A., Eitelberg, G., and Veldhuis, L. L. M., “Wingtip-Mounted Propellers: Aerodynamic Analysis of Interaction Effects and Comparison with Conventional Layout,” *Journal of Aircraft*, Vol. 56(1), 2018, pp. 295–312. doi:10.2514/1.C034978.
- [53] Deere, K. A., Viken, J. K., Viken, S. A., Carter, M. B., Cox, D., Wiese, M. R., and Farr, N., “Computational Component Build-up for the X-57 Distributed Electric Propulsion Aircraft,” 2018 AIAA Aerospace Sciences Meeting, Kissimmee, FL, USA, January 8-12 2018. doi:10.2514/6.2018-1275.
- [54] European Aviation Safety Agency, “Certification Specifications and Acceptable Means of Compliance for Large Aeroplanes,” CS-25/Amendment 21, 2018.
- [55] IHS, “Jane’s All the World’s Aircraft,” , accessed December 2018. URL <https://janes.ihc.com>.
- [56] Gerssen-Gondelach, S. J., and Faaij, A. P. C., “Performance of batteries for electric vehicles on short and longer term,” *Journal of Power Sources*, Vol. 212, 2012, pp. 111–129. doi:10.1016/j.jpowsour.2012.03.085.
- [57] Stückl, S., “Methods for the Design and Evaluation of Future Aircraft Concepts Utilizing Electric Propulsion Systems,” PhD Dissertation, Technische Universität München, 2016.
- [58] Lents, C., Hardin, L., Rheame, J., and Kohlman, L., “Parallel Hybrid Gas-Electric Geared Turbofan Engine Conceptual Design and Benefits Analysis,” 52nd AIAA/SAE/ASEE Joint Propulsion Conference, Salt Lake City, UT, USA, July 25-27 2016. doi:10.2514/6.2016-4610.
- [59] Bijewitz, J., Seitz, A., and Hornung, M., “A review of recent aircraft concepts employing synergistic propulsion-airframe integration,” 30th Congress of the International Council of the Aeronautical Sciences, Daejeon, Korea, September 25-30 2016.